

2014-01-01

# A Study Of Ti-Doped WO<sub>3</sub> Thin Films Using Comparative Theoretical And Experimental Approach

Aurelio Paez

University of Texas at El Paso, aurelio.paez@gmail.com

Follow this and additional works at: [https://digitalcommons.utep.edu/open\\_etd](https://digitalcommons.utep.edu/open_etd)

 Part of the [Materials Science and Engineering Commons](#), [Mechanics of Materials Commons](#), and the [Physics Commons](#)

---

## Recommended Citation

Paez, Aurelio, "A Study Of Ti-Doped WO<sub>3</sub> Thin Films Using Comparative Theoretical And Experimental Approach" (2014). *Open Access Theses & Dissertations*. 1697.

[https://digitalcommons.utep.edu/open\\_etd/1697](https://digitalcommons.utep.edu/open_etd/1697)

This is brought to you for free and open access by DigitalCommons@UTEP. It has been accepted for inclusion in Open Access Theses & Dissertations by an authorized administrator of DigitalCommons@UTEP. For more information, please contact [lweber@utep.edu](mailto:lweber@utep.edu).

A STUDY OF TI-DOPED WO<sub>3</sub> THIN FILMS USING COMPARATIVE THEORETICAL  
AND EXPERIMENTAL APPROACH

AURELIO PÁEZ

Department of Physics

APPROVED:

---

Felicia S. Manciu, Ph.D., Chair

---

William Durrer, Ph.D.

---

Eric Hagedorn, Ph.D.

---

Marian Manciu, Ph.D.

---

Stella Quinones, Ph.D.

---

Bess Sirmon-Taylor, Ph.D.  
Interim Dean of the Graduate School

Copyright ©

by

Aurelio Páez

2014

## **Dedication**

I would like to dedicate this thesis to myself, my brain, and the makers of coffee.

A STUDY OF TI-DOPED WO<sub>3</sub> THIN FILMS USING COMPARATIVE THEORETICAL  
AND EXPERIMENTAL APPROACH

by

AURELIO PÁEZ, B.S.

THESIS

Presented to the Faculty of the Graduate School of

The University of Texas at El Paso

in Partial Fulfillment

of the Requirements

for the Degree of

MASTER OF SCIENCE

Department of Physics

THE UNIVERSITY OF TEXAS AT EL PASO

May 2014

## **Acknowledgements**

I want to express my appreciation to my advisor, Dr. Felicia Manciu. Her advice and patience with me while I was performing research and graduate studies has impacted me on a deep personal level. My graduate career salvaged by the faith she had in me, more than once. Thank you.

I also want to thank the committee members, Dr. William Durrer, Dr. Marian Manciu, Dr. Stella Quinones, and Dr. Eric Hagedorn. Each and every one of you has helped me in some special way that words cannot express and in ways I can't describe. Thank you for attending my defense and your interesting and thoughtful comments and questions.

I want to thank my father, whose support allowed me to pursue my lifelong dream. Thank you, Pops. Without your help I would not have come this far. Without your friendly conversations and motivational speeches I could not have accomplished this.

To my children I give the warmest of apologies and thanks for being perfect children to an imperfect father. I wasn't always there when you needed me. I hope to remedy that for the rest of my life if you will let me.

To my brother, both our struggles were very different these past years. I read books, you dodged bullets. Thank you for your belief in me. Our phone calls and correspondence kept me sane. We are better men for this time in our lives.

To the God King Alexander I want to thank for being my friend longer than anyone else ever has. "Don't believe in yourself. Believe in me who believes in you."

## **Abstract**

Metal oxides like Tungsten Oxide ( $\text{WO}_3$ ) are well documented and characterized in the literature, with uses in darkening windows and mirrors, flat computer displays, solar panel cooling, and sensors (of interest in this study). Ti doping of  $\text{WO}_3$  is less documented and the focus of this study. Sample thin films of pure  $\text{WO}_3$  and varyingly Ti doped  $\text{WO}_3$  were prepared using Radio Frequency magnetron sputtering (RF) (13.56 MHz) to grow thin films on a silicon substrate. This study aims to compare multiple Ti doping percentages in  $\text{WO}_3$  theoretically and then compare with experimental data taken from thin films of various Ti doping levels grown at temperatures ranging from room temperature to 400  $^{\circ}\text{C}$ . Characterization of the materials was to be conducted using Fourier Transform Infrared Spectroscopy, Raman Spectroscopy, X-ray diffraction, and other theoretical and simulated approaches. Theoretical calculations optimized Ti doping at somewhere between 6.25% and 12%. Experimental data indicates that under the given growing conditions optimal Ti doping is 5%. The percentage of Ti may be able to be increased and the material retain desired characteristics with an increased growth temperature above 400  $^{\circ}\text{C}$  as annealing samples post-growth has no positive impact on the thin film structure.

## Table of Contents

Acknowledgements.....	v
Abstract.....	vi
Table of Contents.....	vii
List of Tables .....	ix
List of Figures .....	x
Chapter 1: Introduction.....	1
1.2.0 Background and Motivation .....	3
1.3.0 Doped Metal Oxide Properties .....	7
Chapter 2: Experimental Details.....	10
2.1.0 Introductory remarks .....	10
2.2.0 Raman Spectroscopy .....	11
2.2.1 Quantum approach.....	11
2.2.2 Introduction to spectroscopic methods .....	12
2.3.0 Fourier transform infrared spectroscopy .....	15
2.4.0 Sample Preparation.....	19
Chapter 3: Results and Discussion .....	21
3.1.0 Introductory remarks .....	21
3.2.0 Computational XRD analysis of standard WO <sub>3</sub> structural phases.....	22
3.3.0 Computational XRD analysis of WO <sub>3</sub> with different Ti doping amounts.....	29
3.4.0 Correlation of computed and experimentally obtained XRD .....	31
3.5.0 Raman analysis of Ti 8% doped WO <sub>3</sub> thin films.....	34
3.6.0 Infrared absorption results of Ti 8% doped WO <sub>3</sub> thin films.....	37
3.7.0 Correlation of computed and experimentally obtained infrared results for Ti doping .....	37
3.8.0 Concluding remarks.....	40
Chapter 4: Conclusion .....	41
4.1.0 Concluding remarks.....	41



References.....	44
Vita.....	47

## List of Tables

Table 1.1: Monoclinic $\text{WO}_3$ atomic coordinates represented in unit cell lengths with lattice parameters of $a = 7.30 \text{ \AA}$ , $b = 7.53 \text{ \AA}$ , and $c = 7.68 \text{ \AA}$ , with $\beta = 90^\circ 54'$ [after ref. 19]. .....	23
Table 1.2: Orthorhombic $\text{WO}_3$ atomic coordinates represented in unit cell lengths with lattice parameters of $a = 7.341 \text{ \AA}$ , $b = 7.570 \text{ \AA}$ , and $c = 7.754 \text{ \AA}$ [after ref. 17]. .....	24
Table 1.3: Tetragonal $\text{WO}_3$ atomic coordinates represented in unit cell lengths with lattice parameters of $a = 5.295 \text{ \AA}$ and $c = 3.928 \text{ \AA}$ for tetragonal phase of $\text{WO}_3$ . [after refs. 18,19] .....	25

## List of Figures

Figure 1: Energy level diagram in Raman scattering..	12
Figure 2: <i>alpha 300R WITec</i> confocal Raman system.....	14
Figure 3: <i>Bruker IFS 66v</i> Fourier transform interferometer (FTIR).....	15
Figure 4: Schematic view of <i>Bruker IFS 66v</i> optical path. (courtesy of Bruker Inc.).....	16
Figure 5: Schematic representation of incident, reflected, and transmitted light. ....	18
Figure 6: Model of $\text{WO}_3$ unit cell for monoclinic structure and XRD spectrum (W –Blue; O-Red)Miller indices included for the monoclinic structure.....	23
Figure 7: Model of orthorhombic structure $\text{WO}_3$ unit cell and XRD spectrum (W – blue; O – Red) Miller indices included for the orthorhombic structure. [after ref. 20]. ....	24
Figure 8: Model of Tetragonal $\text{WO}_3$ unit cell and XRD spectrum (W – Blue; O – Red) Miller indices included for the tetragonal structure. [after refs. 18,19].....	25
Figure 9: Characteristic X-ray diffraction spectra for monoclinic (red), orthorhombic (blue), and tetragonal (green) $\text{WO}_3$ structures with $2\theta$ values ranging from about $22^\circ$ to $26^\circ$ . ....	26
Figure 10: Experimental XRD results obtained for pure $\text{WO}_3$ thin films (black) with characteristic X-ray diffraction spectra for monoclinic (red), orthorhombic (blue), and tetragonal (green) $\text{WO}_3$ structures. ....	27
Figure 11: XRD spectra for 3% Ti doped $\text{WO}_3$ (black), monoclinic (red), and tetragonal (green) structures.. ....	28
Figure 12: Theoretical X-ray diffraction spectra of $\text{WO}_3$ and 1.5% Ti doped $\text{WO}_3$ .....	30
Figure 13: Computed XRD spectra for Ti doped $\text{WO}_3$ at the following percentages	

12.5% (red), 6.25% (green), and 1.5% (black) of Ti .....	31
Figure 14: XRD spectra for experimental and simulated data for 5% Ti doping (black) and 6.25% Ti (red) of $\text{WO}_3$ .....	32
Figure 15: Theoretical XRD spectra for $\text{WO}_3$ with 12.5% Ti doping (red) and for the tetragonal $\text{WO}_3$ morphology (black). .....	33
Figure 16: 8% Ti Doping Raman Spectra for $\text{WO}_3$ samples of varying Si substrate growth temperatures, RT, 200 °C, 400 °C .....	35
Figure 17: Multiple percentage Ti-doped $\text{WO}_3$ samples Raman spectra, grown at 400 °C substrate temperature.....	36
Figure 18: Pure $\text{WO}_3$ and Ti-doped $\text{WO}_3$ IR absorption spectra for samples grown at 400 °C substrate temperature .....	38
Figure 19: (a) Experimental transmission data for pure $\text{WO}_3$ (blue) and 5% Ti doping of $\text{WO}_3$ (red) (b) Simulated absorption infrared vibrational lines for pure $\text{WO}_3$ (blue) and 12.5% Ti doping of $\text{WO}_3$ (red).....	39

## Chapter 1: Introduction

### 1.1.0 Remarks

This research into Titanium doped Tungsten Oxide (Ti-WO<sub>3</sub>) spurs from the need for better materials to improve sensor capabilities of sensors used in Integrated Gasification Combined Cycle coal power plants. This research was supported by a grant from the DoE to widen the breadth of knowledge on material candidates for use in the detection of poisonous gases produced in the burning of coal, during energy production. Research into transition metal oxides stems from the discovery of their electro, photo, and thermo chromic properties. These oxides are in common use in darkening windows, darkening mirrors, flat screen televisions, etc. In addition WO<sub>3</sub> can be layered easily over large surfaces, making it easy to implement in manufacturing. Considering that some transition metal oxides can convert heat into electrical current, it is not a far stretch to think that they might be able to help capture waste heat in manufacturing. The value of study and research into transition metal oxides is apparent.

Coal Gasification, as a process, is a very harsh environment for sensors. Usable sensors need to be robust, handle high temperatures, have quick response, and be produced by a repeatable process. Thus this research looks to expose the physical properties of WO<sub>3</sub>, doped and un-doped, and the effect of growth methods, various doping percentages, and microstructures on the lab grown thin films in a systematic and pragmatic way. This research does not include device production or development.

This research should provide a comparison of various doping percentages, in detailed microscopic and spectroscopic properties of tungsten oxide doped with Ti from 0% to 20%. Techniques used in the lab included Raman spectroscopy, Fourier Transform Infrared Absorption Spectroscopy (FTIR), and X-Ray diffraction (XRD). This research was funded by a grant from the Department of

Energy to further the advancements in the materials used in sensors used for detecting toxic chemicals involved in coal-gasification plants.

The United States has abundant reserves of coal. However, the interest in cleaner energies and reduction of carbon footprints has led to efforts to develop lower pollution coal burning. This has led to the development of the Integrated Gasification Combined Cycle (IGCC). IGCC offers to lower pollution emissions while giving better efficiency and energy production. This cycle produces dangerous byproducts that have to be tested and probed for throughout the gasification process. It is estimated that IGCC can reach 55% efficiency with a reduction of emissions that is measured in orders of magnitude below steam power plants of the past {1}. However, this poses a need for monitoring and reaction to data from the sensors by power plant employees. As such the need for sensors and sensor materials with high-sensitivity and selectivity with real time detection capabilities cannot be over stated. {2}

Coal-gasification requires the heating of coal to high temperatures and under high pressures in order to extract Hydrogen gas from coal and steam. This environment necessitates that the materials used in sensors be tolerant of such environments. Although the sensors and sensor packaging are beyond the scope of the grant, the search for a reliable material must be approached systematically; specifically, by determining the effect of processing conditions on the growth and microstructures of thin films. First un-doped  $\text{WO}_3$ , and then various percentages of Ti-doped  $\text{WO}_3$  are to be tested, revealing properties and stable microstructures.

These Microstructures are incredibly small. The conglomeration of all tests and procedures conducted in the lab in order to understand the nature of the infinitesimally small is called “Material Characterization”. This concept of characterization applies to physical testing and/or analysis of collected data. If there are “fathers” of the material science of material characterization they would be William Lawrence Bragg, and Sir Chandrasekhara Venkata Raman. Bragg, famous for Bragg’s law and the invention of X-ray crystallography, and Sir Raman, who is known for the discovery of Raman

scattering, which is the inelastic scattering of light and the basis of Raman spectroscopy, a pillar in Material Characterization.

What follows is a breakdown of prior studies, research, and interest in the science of metal oxides. The development of these materials is for gas sensing sensors, and for enhancing their exploitable properties. This research is focused on Ti-doped WO<sub>3</sub>, specifically properties, microstructures, ideal doping percentages and thin film growth criteria.

## **1.2.0 Background and Motivation**

Originally synthesized by Robert Oxland in 1841, WO<sub>3</sub> has spurred interest in the scientific community for the development of applications for WO<sub>3</sub>. Due to its electrochromic and photochromic properties WO<sub>3</sub> was looked at for one of these optical properties, reacting to a current by darkening. This reversible effect on the crystal was integrated into current technologies such as camera displays, auto-darkening rear view mirrors, and smart windows that change the amount of light and energy entering a building. Of course this improves comfort levels but also reduces the carbon foot print. In order to regulate the opacity of the thin films, the films thickness was varied or coloration of the film through electrochemical processes. As novel as the darkening glass was, later scientific inquiry became interested in using the films' electrochromic properties in gas sensing.

Attempts by Huang et al [3] were attempting to create UV photodetection nanowire elements eventually dovetailed into development of high-sensitivity nanoscale detectors and switching devices. The team accomplished this via hydrothermal coating of a nanowire with WO<sub>3</sub>. As the team created these nanowires and began testing, something interesting came to light. Optical absorptivity and electrical conductivity increased.

Sensors using Metal Oxides (MOX) are many decades old and are widely used in the detection of toxic and/or combustible gases. These sensors are reliable, low cost, and implement easily.

Considering that the common chemical in the sensors is oxygen it can be seen that it is oxygen that is the source of the detection mechanisms at the sensor surfaces. One can imagine the sensor's surface adsorbing more or less oxygen ions from the atmosphere, contingent on environmental factors. Different concentrations of adsorbed oxygen remove electrons from the MOX sensor and create potential barriers that limit electron movement, which in turn affects conductivity. As reactive gasses combine with the oxygen adsorbed on the surface the oxygen ion is removed, the electron is replaced in the MOX sensor, causing the potential barriers to lower and thus increasing conductivity.

These sensors marry the chemical world to the electronic world as described above, wherein a change in the chemistry results in a change of electronic signal. Apart from producing the correct science sensors must also;

- Be Highly sensitive to substances to be detected
- Be physically small and Economical
- Ability to detect multiple chemicals or physical properties
- Keep the Minimum interactive distance with the substance being measured
- Maintain mechanical structure for long hours of operation
- Produce predictable and reproducible electrical effects {4}

Thin Film sensors resolve many of the problems that occur with ceramic sensors and thick film sensors. Thin films tend to use less power, are less susceptible to humidity changes, temperature changes, and are more consistent from one unit to another.{4} All these qualities make them tempting for use in Coal Gasification plants where temperatures can be incredibly high with exposure to water vapor, and which require sensitivity and reliability. {5}  $\text{WO}_3$  is an N type semiconductor, meaning that it has an excess of metal molecules present when compared to ideal stoichiometry ratios. As mentioned before all of the interactions occur at the surface and this should not be surprising as the surface area is large relative to the bulk of the film. It is conductivity that changes depending on chemicals at or around the surface. The



behavior is attributed to oxygen vacancies in the metal excess material. The concept is known as the Schottky barrier at interparticle distances and attempts to describe the mechanics of the Oxygen at the surface attracting surrounding electrons. {5}

Thin Film benefits are obvious; however there are many semiconducting oxide materials like  $\text{WO}_3$ ,  $\text{TiO}_2$ ,  $\text{SnO}_2$ ,  $\text{ZnO}$ ,  $\text{In}_2\text{O}_3$  and  $\text{Fe}_2\text{O}_3$ . There are also Catalytic Oxides such as  $\text{VO}$ ,  $\text{MoO}_3$ ,  $\text{CuO}$ , or  $\text{NiO}$ . Many of these have been used for decades and merit a small aside as a view of the progression of oxide materials.

One of the earliest, and most used, materials used in gas detection is  $\text{ZnO}$ . At 25% sensitivity to  $\text{NH}_3$  at 30 ppm research has been done to try to augment the sensitivity. Reducing the size of the nanoflakes, annealing the samples, and raising operating temperatures have all been attempted to try to boost performance of  $\text{ZnO}$ . When humidity became a concern  $\text{SnO}_2$  was studied. It was shown that  $\text{SnO}_2$  reduced the effect of moisture and humidity on CO detection and more recently combinations of  $\text{ZnO}$  and  $\text{SnO}_2$  show better improvements. CO detection in this study was performed at 50-500 ppm and between 250 and 400 degrees C {6}. Studies have also shown when potential oxide materials begin to experience issues with sustained use of the kind that would be typical in coal gasification. For example  $\text{In}_2\text{O}_3$  films are most sensitive to ethanol detection at 80 ppm and at a temperature of 350 C. The study revealed that the higher temperatures and exposure to gas resulted in degradation of the  $\text{In}_2\text{O}_3$  structure. The migration of the In atoms was found to be minimized by making the thin films thinner. The thinner film needed less current to detect surface chemistry and consequently caused less electro-migration of the In atoms {7}. One dimensional  $\text{In}_2\text{O}_3$  wires have shown even more improvement. Continuing the trend of smaller materials, nano-structured  $\text{TiO}_2$  is used in gas sensors sensing 20 ppm  $\text{NO}_2$  in exhaust pipes at normal operating temperatures for the environment {8}.

This thesis focus is  $\text{WO}_3$ . It has advantages in both the metal oxide and semiconducting oxide categories. Although  $\text{WO}_3$  has been shown to be less efficient at detecting carbon monoxide,

hydrocarbon, and other Volatile organic compounds (VOC) than other oxide materials, it has been a candidate for sensing O<sub>3</sub>, NO<sub>2</sub>, NH<sub>3</sub>, H<sub>2</sub>, and H<sub>2</sub>S.

Volcanoes are known to vent H<sub>2</sub>S just before eruption. H<sub>2</sub>S is highly toxic and in concentrations of 250 ppm is deadly to humans. Produced as a byproduct of many chemical processes and combustion it is polluting the atmosphere. Venus's atmosphere has a major concentration of H<sub>2</sub>S. The gas also reacts explosively when exposed to temperatures of 260 C {9}. In all these situations WO<sub>3</sub> metal oxide sensors would be ideal choices.

WO<sub>3</sub> semiconductor metal oxide sensors have great potential for the sensing of H<sub>2</sub>S. WO<sub>3</sub> films produced with the RF sputtering technique are well suited for H<sub>2</sub>S detection as they are sub-stoichiometric. WO<sub>3</sub> peak sensitivity was found to be at 475 K. In the case of thick film versus thin film, it has been found that the thin film resistance dropped as the film reacted with chemicals in the atmosphere. A thick film's resistance increases in similar situations thus causing more power consumption. This adaptation of the conductivity is thought to be a product of steady state concentration of oxygen vacancies on the surface of the sensor. Also studied is the WO<sub>3</sub> sensors ability to operate in varying levels of humidity from dry to wet. The WO<sub>3</sub> sensors sensitivity to H<sub>2</sub>S was studied and found to vary greatly from one sensor to another, even within the same array of sensors. This occurred with RF sputtered WO<sub>3</sub> thin films. Some were even found to be detecting at ppb without gold doping. However, the increased humidity increased the conductivity of the WO<sub>3</sub> films. This interfered with detection of the H<sub>2</sub>S gas.

It is obvious that metal oxide sensor capabilities, sensing properties, and characteristics are contingent on stoichiometry, nanoporosity, grain size, crystallinity, nano structure, etc. Within the scope of this research we will try to understand how the amount of surface vacancies correlates with doping percentages. This surface structure and chemistry change due to doping has an effect on Oxygen vacancies that helps in the adsorption of oxygen. It is necessary to discuss all the properties of pure

WO<sub>3</sub> prior to beginning the conversation about doping. In the next section we discuss spectroscopic, structural, and known properties of unadulterated WO<sub>3</sub>.

### 1.3.0 Doped Metal Oxide Properties

As the World's energy needs increase scientists and engineers must find new ways to produce electricity. In 1996 the Department of Energy backed the opening of a new type of power station. Polk Power station in Florida produces electricity using coal. This modern technique combines many techniques for improved Clean Coal energy. IGCC (*integrated gasification combined cycle*) begins with coal powder and water mixed into a slurry similar to heavy oil. This slurry is super heated and pollutants captured. Every attempt to recapture heat is made. This type of forward thinking coal burning reduces emissions and boosts the efficiency of a coal burning plant. However, the environment inside the plant during gasification has high humidity and a high temperature upwards of 1200 Kelvin {2}. This should indicate the types of properties needed for sensors that will be used in a coal gasification plant. Any sensor has to be able to withstand high temps, and have good sensitivity, selectivity, and stability, collectively known as 3S. This need for better sensors has driven the investigation of metal oxides, and subsequently, doping of such metal oxides with materials that will increase the desired properties of the material investigated. What follows are examples of studies conducted to find useful physical and spectroscopic properties for sensing purposes.

A way of attacking the problem of Energy is to reduce consumption. Reducing the amount of light that can pass through a window in a house or vehicle can reduce the energy required to cool the interior. Tungsten Oxide is transparent with a band gap of 2.62eV {5}. Moreover it is known that infrared absorption increases when free electrons are introduced into the crystal. In the case of heat shielding for solar panels or windows, one study sought to decrease infrared light transmission while allowing as much visible light as possible to get through. In this case the tungsten oxide was doped with

Na, Ti, Rb, and Cs. The study revealed that the addition of nanoparticle doping to the  $\text{WO}_3$  transmitted around 85% of the visible spectrum while keeping a solar heat gain coefficient of 0.59 {10}.

As previously stated the temperatures that  $\text{WO}_3$  sensors will be exposed to are very high.  $\text{WO}_3$  undergoes a change when annealed. As shown by Lee et.al. in a study on the effects of annealing  $\text{WO}_3$  for photovoltaics {11}, annealing significantly improved the performance of their photovoltaic devices. Their devices saw an improvement in power conversion efficiency, fill factor, short current density, and open voltage, with an overall effect of decreasing series resistance. Lee contributed some of the beneficial changes to the fact that the annealing had a smoothing effect on the surface morphology of the  $\text{WO}_3$ . Additionally, the annealed  $\text{WO}_3$  samples became hydrophobic, which would be beneficial in high humidity environments.

The previous study mentioned annealing to  $350^\circ\text{C}$ . A study on the microstructural effects of annealing to higher temperatures on  $\text{WO}_3$  grown by radio frequency magnetron sputtering showed a change in morphology. The study showed that the thin film was changing from amorphous to crystalline at  $315^\circ\text{C}$ . In addition to testing the higher annealing temperature the study tested concentrations of doping using gold, platinum, and palladium. Annealing had several effects, to include increasing stability and sensitivity; however, decreasing film conductivity. This decrease in conductivity has to do with surface morphology changes due to annealing the samples at greater than  $400^\circ\text{C}$ . The induced crystallization of the surface provoked an improvement in the sensitivity of the thin film to  $\text{H}_2\text{S}$  {12}. Hydrogen Sulfide is a byproduct in the IGCC coal gasification process and must be monitored {1}. Using Gold doped  $\text{WO}_3$  a sensitivity of parts per billion to  $\text{H}_2\text{S}$  has been achieved {13}. Deviations from stoichiometry ratios can lead to defects in the morphology of the film, however M.D. Antonik et.al. note that this type of defect does not impact their study.

Stoichiometric ratios do play a role in Metal Oxide applications. In the case of  $\text{WO}_3$ , non-stoichiometric  $\text{WO}_{3-x}$  exhibits superior performance created by the defects of Oxygen vacancies. Su et.al

were able to manipulate the growth of  $\text{WO}_3$  films to reach sub-stoichiometric ratios by manipulating plasma current, chamber pressure, and the oxygen partial pressure.

Metal oxide films are important components in all aspects of sensors and sensing. The characteristics we are looking for are influenced by stoichiometry, morphology, composition, and crystallinity. With this in mind, spectroscopy, microscopy, and structural studies are to be presented. This will let us characterize Titanium doped  $\text{WO}_3$ .

## Chapter 2: Experimental Details

### 2.1.0 INTRODUCTORY REMARKS

Optical spectroscopy is by definition the study of matter's interaction with light (a form of electromagnetic energy). The data collected are called "spectroscopic data" that we also call spectrums, or response plots. Many types of techniques are included under the umbrella of spectroscopy in general. Techniques like Raman, Fourier transform infrared absorption spectroscopy (FTIR), X-ray photoelectron spectroscopy (XPS), X-ray diffraction (XRD), Atomic Force Microscopy (AFM), and Scanning Electron Microscopy (SEM) are just a few that compose the suite of techniques that is "*Spectroscopy*." No single technique can tell us everything about a test sample, thus requiring the scientist to use a set of these techniques. Each technique tests for certain properties or aspects of a material. Certain techniques complement each other better than others. One such pair of techniques is Raman and FTIR, since both are investigating the vibrational modes of a given material. To study all these modes, which are a result of a material absorbing infrared radiation, FTIR is mainly used for non-symmetrical vibrational state analysis. Raman spectroscopy will complement this analysis well, as it tests for the inelastic collisions of photons in the material, being mainly sensitive to symmetrical vibrational states.

Within materials there exist vibrational modes that are unique to that material. For inhomogeneous materials, each constituent substance has its unique vibrational spectrum that allows for both qualitative and quantitative analysis. Regarding Raman spectroscopy the spectrum plots of intensity versus wavenumber are very specific and repeatable.

## 2.2.0 Raman Spectroscopy

The current Raman spectroscopic data was collected in the *Optical Spectroscopy & Microscopy Laboratory* of the Department of Physics. The instrument used was an *alpha 300R WITec* confocal Raman system, with a 532 nm excitation of a Nd:YAG laser.

Raman spectroscopy is named after Sir Chandrasekhara Venkata Rāman whom discovered that some of the light traversing transparent material will deflect and change in wavelength. Thus, when light interacts with a material, photons strike molecules within the material and are deflected through inelastic scattering. Raman spectroscopy is based on these inelastic scattering events. The effect of inelastic scattering is called Raman Effect, or Raman scattering. The actual percentage of light that changes wavelength is very small ( $\sim 10^{-6}$ ).

When the wavelength of the outgoing photon is the same as the incoming photon, another effect takes place, named Rayleigh scattering or elastic scattering. Incidentally, Rayleigh scattering (and the lack of purple sensors in the human eye) is the reason the sky is blue.

### 2.2.1 Quantum approach

Within test samples there are molecular structures, crystal structure, and other chemical groups affecting the scattered photons. A scattered photon can have a higher or lower energy, as pictorially presented in Figure 1. If the photon strikes one of the above structures and causes this structure to excite into a virtual quantum state, when the structure returns to its ground state it will re-emit the photon with less energy, thus changing its wavelength. This change in wavelength is on the order of a few wavenumbers ( $\text{cm}^{-1}$ ). If the scattered photon encounters a structure that had a higher energy to begin with, the structure re-emits the photon with a higher wavelength. Looking at the spectrum, lower energy

spectral lines are called Stokes spectral lines. When they are higher in energy they are named Anti-Stokes lines.

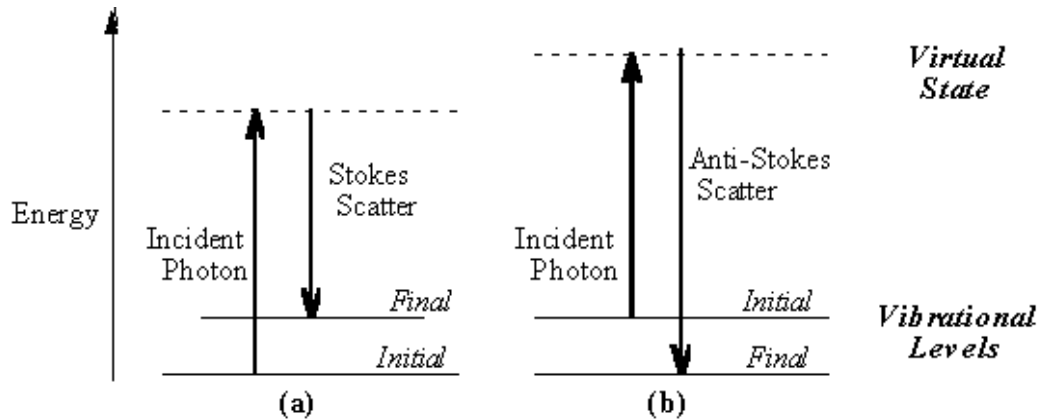


**Figure 1:** Energy level diagram in Raman scattering. [14]

Either case is illustrating the energies of the vibrational states of the structures. Thus, the repeatability and precision of the Raman technique allows for ease of analysis to meet both the quantitative and qualitative needs of the project by analysis of the Raman spectra fingerprints.

## 2.2.2 Introduction to spectroscopic methods

For vibration to be Raman active, it must occur with a change in the polarizability of the molecule. A detailed explanation of this process is as follows: when the electric field component of the electromagnetic radiation (light) is interacting with a molecule, it will induce a dipole moment. This induced dipole moment, which is a vector, and the electric field are related by a property called polarizability, as described by the relation below [15]:

$$p = \alpha(Q) \cdot E = \alpha(Q) \cdot E_0 \cos(\omega_L t) \quad (1)$$



where  $p$  is the dipole moment,  $\alpha$  is the polarizability, and  $E$  is the electric field which has a maximum amplitude of  $E_0$  and depends on the light's angular frequency  $\omega_L$ .

Also, polarizability, which is a tensor depending on the vibrational coordinate  $Q$ , is a measure of the deformability of the electron cloud of the molecule by the electric field. The vibrational coordinate,  $Q$ , depends on the molecular vibrational angular frequency,  $\omega_M$ , as follows:

$$Q = Q_0 \cdot \cos(\omega_M t) \quad (2)$$

Thus, the change in polarizability gives rise to amplitude modulation, at certain frequencies, of the induced dipole moment oscillation, which gives rise to the Raman frequency components. [2] This statement is easier understood if the Taylor series expansion of the polarizability:

$$\alpha = \alpha_0 + \left[ \frac{\partial \alpha}{\partial Q} \right] \cdot Q + \dots \quad (3)$$

is substituted into the expression of the induced dipole moment (Eq. (1)) to obtain the first-order expression:

$$\begin{aligned} p &= \alpha_0 \cdot E_0 \cos(\omega_L t) + \left[ \frac{\partial \alpha}{\partial Q} \right] \cdot Q_0 \cdot E_0 \cos(\omega_M t) \cos(\omega_L t) \\ p &= \alpha_0 \cdot E_0 \cos(\omega_L t) + \left[ \frac{\partial \alpha}{\partial Q} \right] \cdot \frac{Q_0 \cdot E_0}{2} [\cos(\omega_L - \omega_M t) + \cos(\omega_L + \omega_M t)] \end{aligned} \quad (4)$$

The first term in this expression for the induced dipole moment (Eq. (4)) has the frequency of the scattered light the same as that of the incident light and this term describes what is called Rayleigh scattering or elastic scattering. The other two terms are for scattered light at lower and higher frequencies, respectively, and their respective effects are called Stokes and anti-Stokes scattering.

Raman Spectroscopy is a research technique that is not affected by water, air, or glass sample holders. Its usage has seen an increase since the advent of the monochromatic laser. Data collection can be done at room temperature, without vacuum, with minimal consideration for interference. If needed, temperature dependence analysis can be performed too. The *alpha 300R WITec* system, which is presented in Figure 2, can accept wafer samples that sit on the sample stage of the microscope in the same fashion as normal microscope slides. The system was used in reflection mode. The microscope has selectable objective lenses, that are used with the normal visible spectrum for focusing and approaching the samples safely, and also used with the Nd:YAG laser.

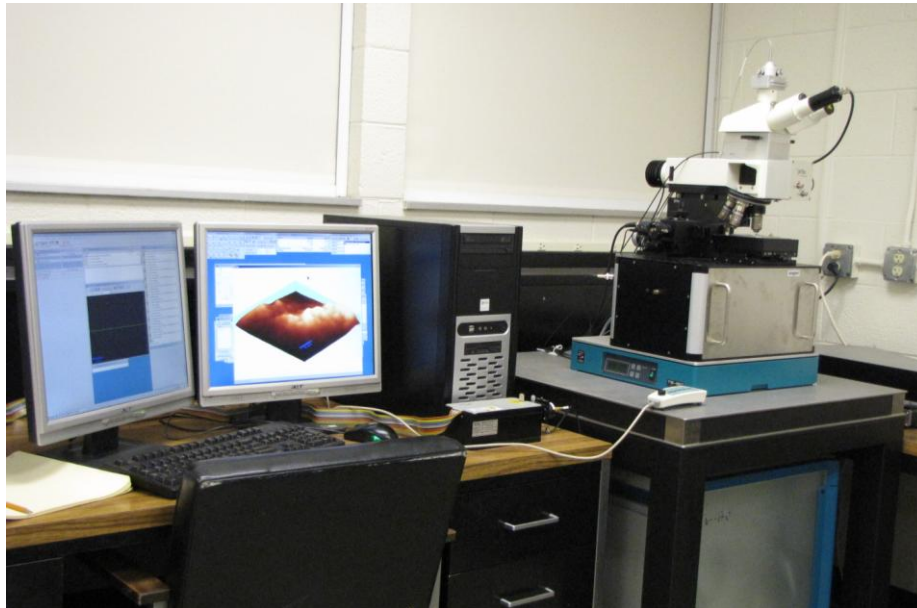


**Figure2:** *alpha 300R WITec* confocal Raman system.

The laser is routed with optical fibers into the microscope that focuses the beam to micron sizes. Upon interaction with the sample, the laser beam undergoes Rayleigh and Raman scattering, as previously mentioned. The optical components within the system filter out all light that is reflected with the same wavelength as the laser. This helps the detector by reducing the unimportant Rayleigh scattered light. The number of counts for Rayleigh scattered light is  $10^6$  times higher than for the Raman scattered light. To prevent damage to the charge coupled device (CCD) a high optical density high pass filter is placed in the path of the returning beam before being routed to the CCD via fiber optics. The system

allows for both single-point Raman spectra or Raman mapping by rastering the laser with sub-micron resolution.

### 2.3.0 Fourier transform infrared spectroscopy

Fourier transform infrared (FTIR) spectroscopy was performed using a *Bruker IFS 66v* system, which works on the principle of a Michelson type of two beam interferometer. A view of the system is presented in Figure 3.

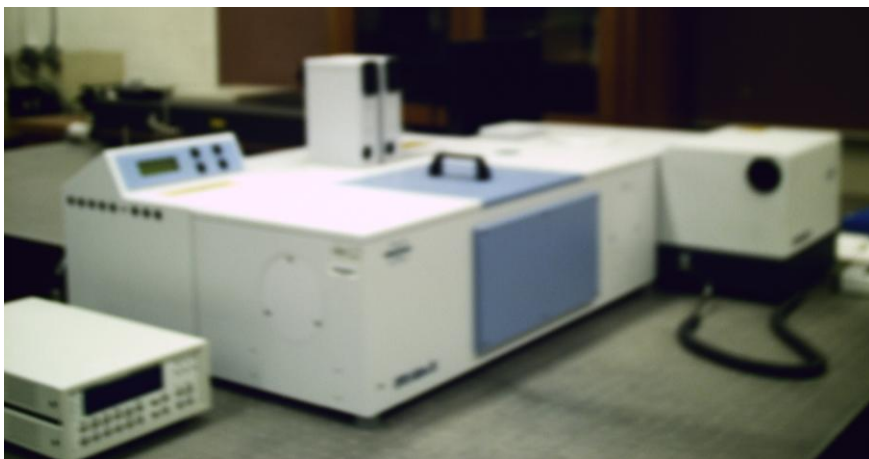


**Figure 3:** *Bruker IFS 66v* Fourier transform interferometer (FTIR).

The *Bruker* system contains a broad spectrum IR source, a beam splitter, two mirrors (one fixed the other mobile), any necessary optics, and a detector. Its schematic optical path is presented in Figure 4.

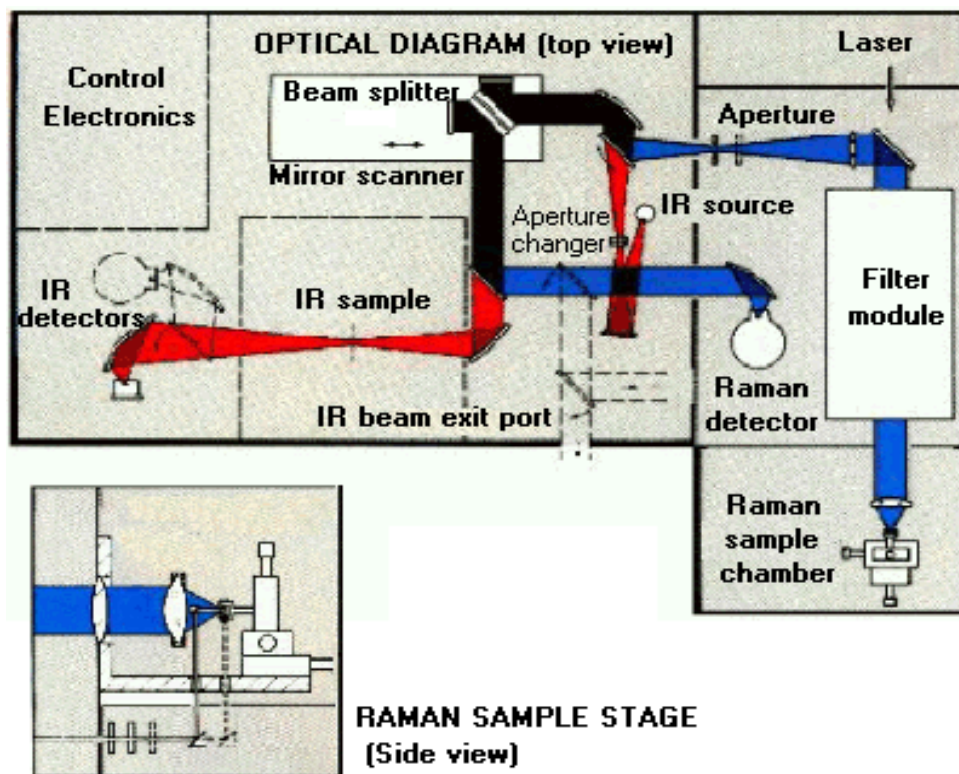


**Figure 4:** Schematic view of *Bruker IFS 66v* optical path. (courtesy of Bruker Inc.)

The idea is to use the broadband infrared source within the interferometer for constructive and destructive light interference to build up a set of data points for different wavelengths. Then the programming can infer what portions of the spectrum were absorbed using a Fourier transform of the data set. The Bruker system can calculate in a time-domain or a space-domain data collection mode.

If the system is set up to perform the Fourier transform as a function of time the system must be set up to record the intensity of radiation as a function of time,  $t$  (that will run from  $-t$  to  $t$ ). The measurements must be made quickly enough so as to simulate a continuous function. A continuous function would be ideal, however the truth of the laboratory is that there will be a finite number of measurements. The approximation function  $f(t)$  of this data set can be written as a Fourier integral where the variable of integration is the angular frequency  $\omega = 2 \pi \nu$  of the infrared source. The Fourier transform of this function is the power spectrum in the angular frequency domain. This is the intensity

of the detected radiation per unit angular frequency. From this, the intensity is known at each frequency. Using photon energy,  $E = h \nu$ ,  $\nu$  being frequency being tested, it is possible to calculate how many photons were detected per unit frequency. Apart from the discrete data set produced, this technique will always be finite in time  $t$ , thus making the function appear to be a periodic function of period  $2T$  with boundary conditions that make the calculation to be of discrete Fourier coefficients. This means that the lowest frequency  $\omega_1 / (2 \pi)$  is equal to  $1/(2 t)$ , and every other frequency is an integer multiple of  $1/(2 t)$ . It is obvious that the more time allowed for data collection, the better the resolution of frequencies is. The system uses the fast Fourier transform (FFT) to compute a set of discrete Fourier integral values per data set per frequency. The time-domain data requires that the mechanical movement of the mirror in the interferometer be very precise and smooth to best collect the data to be used. This adds to the complexity of the experiment.

The *Bruker IFS 66v* system's space-domain data collection is considered as a more robust technique, which is less susceptible to the fragility of the time-domain data collection. In this scenario, rather than using time as the independent variable, the adjustable mirror stops briefly and the system take a data point for this position. The position of the mirror is measured very precisely by use of interference of a helium-neon laser beam inside the interferometer. The intensity of the radiation is measured differently in this approach, since is taken as a function of distance in the interferometer. The Fourier transform becomes a function of  $k = 2 \pi / \lambda$ . Radiation intensity data is recorded for some  $N$  positions. Resolution can be increased by increasing the number of data points per sweep. By increasing the sweep length and maintaining the mirror distance changes fixed, the system increases the  $N$  data points, thus increasing the resolution. Using this data set the FFT plots a power spectrum.

The procedure for measuring the samples is as follows. The samples are produced as thin film deposited on silicon wafers and are used directly instead of samples prepared in the form of pellets. The latter sample preparation process requires crushing the sample, mixing it with a non-absorbing matrix in

the frequency range of interest, and pressing it in form of a pellet with appropriate dimensions. Thus, when thin film materials grown on silicon wafers are measured, besides the transparency of the substrate (silicon in this case) in the selected energy region, the appropriate substrate thickness that allows enough light to reach the detector and avoids over-absorption effects, should be considered.

Since the infrared absorption process is based on the well known Bouguer-Lambert-Beer law of absorption of light:

$$I_T(\nu) = I_0(\nu) e^{-\alpha(\nu) d} \quad (5)$$

where  $I_0$  and  $I_T$  denote the intensities of the incident and transmitted beams at a specific wavenumber ( $\nu$ ),  $\alpha$  is the linear absorption coefficient at a specific wavenumber, and  $d$  is the thickness of the sample, the infrared spectrum is the ratio of  $\frac{I_T(\nu)}{I_0(\nu)}$  that is automatically calculated by the computer.

Schematically the process is shown in Figure 5.



**Figure 5:** Schematic representation of incident, reflected, and transmitted light

Thus, firstly, the data without a sample should be acquisitioned (*e.g.*,  $I_0$ ). This data, also known as background collection, is used to determine what spectrum the broad infrared source has in the particular frequency region. It is also used for system calibration purposes, allowing the interferometer to locate the zero path difference (ZPD). This is the point at which each of the mirrors is located such that the light reaching the detector has traveled the exact same distance over the two distinct paths. This is equivalent to having never split the beam, and as such, is at maximum intensity, when the electromagnetic radiation is in phase for a constructive interference process.

With the sample in place the detector is now recording  $I_T$ . Through computation, the system can perform the ratio of the response of the detector with and without the sample (*i.e.*, the original  $I_0$  spectrum). This data set can be collected by the system in the form of an interferogram, which is subsequently sent to the computer and worked on via FFT to result in a power spectrum. The benefit of FTIR systems is that even with weak signals the system can repeat the experiment and collect data that can be co-added to increase the signal to noise ratio. In the current analysis of the  $\text{WO}_3$  samples, the system was programmed to make 256 scans per measurement.

## 2.4.0 Sample Preparation

The  $\text{WO}_3$  and Ti-doped  $\text{WO}_3$  samples studied in this work were synthesized locally at the University of Texas at El Paso in Dr. Ramana's laboratory in the Mechanical Engineering Department. A radio frequency magnetron sputtering (RF) (13.56 MHz) growth process was used. First, the Silicon substrates were cleaned with isopropyl alcohol and dried with nitrogen. They were introduced into the vacuum chamber with a base pressure of  $\sim 10^{-6}$  torr. Different metal targets, of W and of W-Ti alloy were used. The W target (Plasmaterials, Inc.) was of 3" diameter and of 99.95% purity. The W-Ti alloy targets (Plasmaterials, Inc.) were of 2" diameter and with different contents of Ti, such as 5% and 8%. The targets were placed inside the chamber at a distance of 8 cm from the substrate.

Before deposition commenced, targets were sputtered for 10 minutes using Ar flow only with the shutters closed. A pre-sputtering power of 40 W was applied to the targets while introducing high purity Ar into the chamber, to ignite the plasma. Once ignition of the plasma was achieved the power was increased to 100 W and oxygen was vented into the chamber for reactive deposition. MKS mass flow meters were used to control the gas flow rates of the argon and oxygen sputtering atmospheres, to achieve Ar: $\text{O}_2$  flow ratios of 1:6 for  $\text{WO}_3$  samples and 1:9 for the Ti-doped  $\text{WO}_3$  samples. The time of

deposition was kept constant at 1 hour. The samples were grown at various substrate temperatures, varying from room temperature to 500 °C. The substrate growth temperature was controlled by an Athena X25 temperature controller and heated with Halogen lamps.



## Chapter 3: Results and Discussion

### 3.1.0 Introductory remarks

Motivation for this research stems from the need for sensors, and subsequent sensor materials, used to detect poisonous and or high environmental impact gasses that are produced in the coal gasification processes used in energy production. The purpose of the study was to engineer and characterize materials for said sensors with a focus on enhancing the 3S criteria, sensitivity, selectivity, and stability. This was accomplished by manipulation of the structure and properties at the nano-scale. Of particular interest is the sensitivity to sulfur emissions, usually in the form of hydrogen sulfide.

Reactions on a thin film of  $\text{WO}_3$  with target emission gasses will occur at the surface of the thin film. It is understood that  $\text{WO}_3$ , when annealed, changes its structure. Annealing a sample changes the surface topology, thus increasing surface area and number of detection sites. Doping the  $\text{WO}_3$  thin film can change the structure, resulting in increased stability of the thin film. Previous findings {16-18} show that doping the  $\text{WO}_3$  thin film with Ti during growth resulted in structural changes. Low percentage doping, in the 5% range, grew the samples with higher structural symmetry and narrower crystalline particle size distribution. Higher concentrations of Ti, in the 20% range, created almost amorphous, non-uniform thin films. It is reasonable to continue searching for a Ti doping percentage that maximizes the structural stability of these thin films. It is also reasonable to show through the use of computational analysis what this Ti doping percentage could be.

We set out to show, computationally, the percentage of Ti doping which maximizes structural stability and maximizes the probability of a tetragonal or higher symmetry phase. The goal is to document the material's properties, as tied to structure, and electronic structure changes and their change in stability. We then compare computational results with prior findings to validate the theoretical results.

### 3.2.0 Computational XRD analysis of standard WO<sub>3</sub> structural phases

A material's structural properties can be explored through X-ray diffraction (XRD), as such XRD computational analysis was done for Ti-doped WO<sub>3</sub>. Results follow:

WO<sub>3</sub> is known to have a monoclinic structure at room temperature {19}. Temperature affects the structure of WO<sub>3</sub> such that 11 phases and 4 crystal structures are known;

- Triclinic from 25-30 °C
- Monoclinic form 30-330 °C {19}
- Orthorhombic from 330-740 °C {20}
- Tetragonal from 740-1437 °C {21,22}

The structure of WO<sub>3</sub> is like that of rhenium oxide with two differences, the movement of W from the center of its octahedron structure and a tilt of said WO<sub>6</sub> structure. {19}

This study is interested in three crystalline morphologies of WO<sub>3</sub>. These structures are known {19-28} as; monoclinic (space group P2<sub>1</sub>/n), the orthorhombic (space group P<sub>mnb</sub>), and the tetragonal (space group P4/nmm). Using the Accelrys 4.0 software we obtained representations of the unit cells for these three morphologies, shown with their respective X-ray diffraction spectra in Figures (6-8). Atomic coordinates for the different morphologies are included in Tables (1-3). These are in good agreement with existing literature {19-28}.

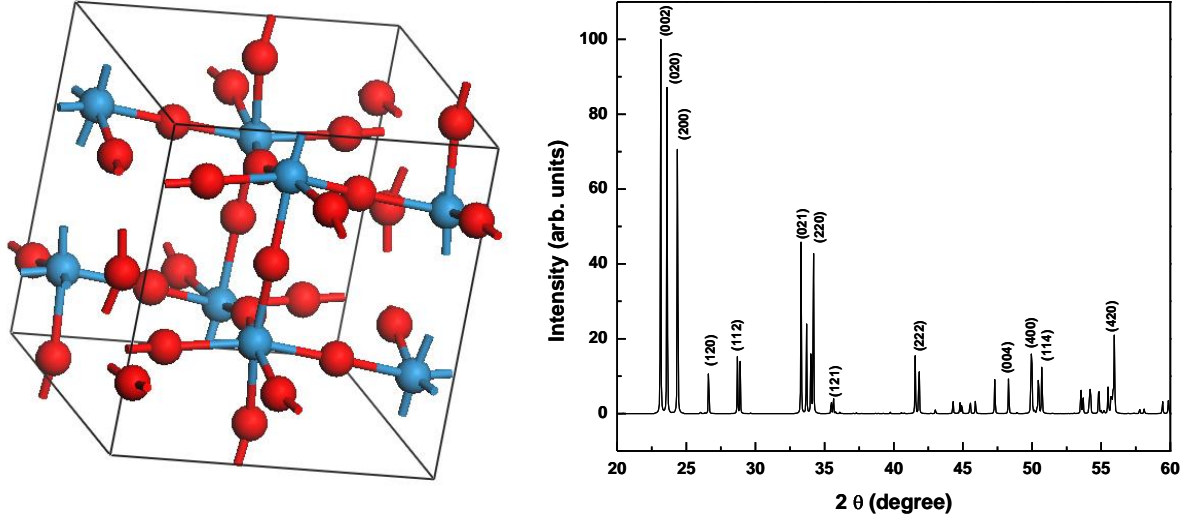


**Figure 6:** Model of  $\text{WO}_3$  unit cell for monoclinic structure and XRD spectrum (W – Blue; O –Red), Miller indices included for the monoclinic structure.

**Table 1.1:** Monoclinic  $\text{WO}_3$  atomic coordinates represented in unit cell lengths with lattice parameters of  $a = 7.30 \text{ \AA}$ ,  $b = 7.53 \text{ \AA}$ , and  $c = 7.68 \text{ \AA}$ , with  $\beta = 90^\circ 54'$  [after ref. 19]

Coordinates /Atom	X	Y	Z
$\text{W}_1$	0.252	0.026	0.0285
$\text{W}_2$	0.247	0.033	0.0781
$\text{O}_{x1}$	0	0.025	0.22
$\text{O}_{x2}$	0	0.475	0.22
$\text{O}_{y1}$	0.29	0.29	0.265
$\text{O}_{y2}$	0.21	0.29	0.735
$\text{O}_{z1}$	0.28	0.040	0.030
$\text{O}_{z2}$	0.28	0.49	0.030

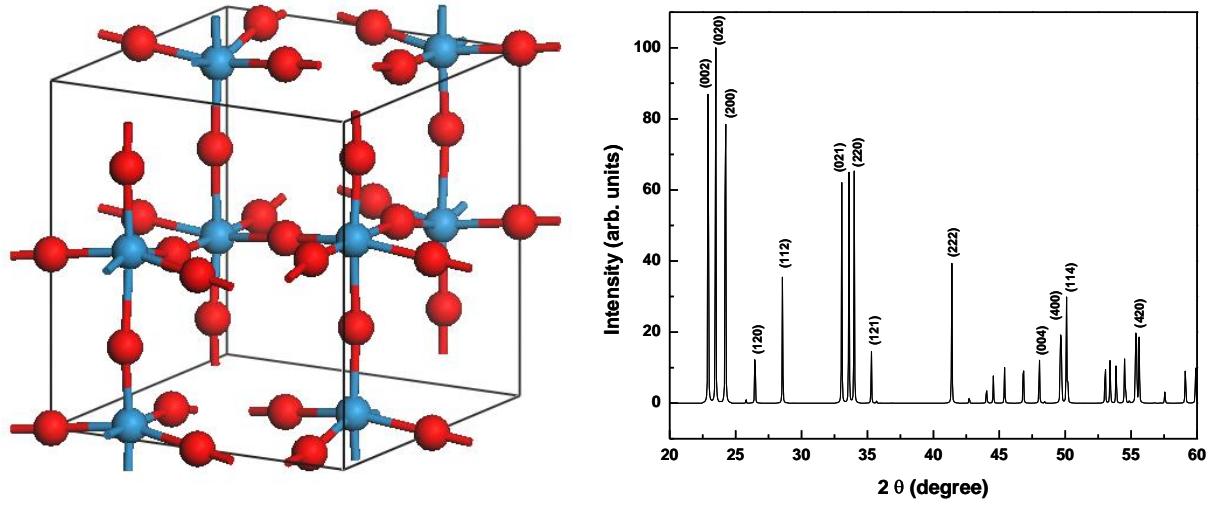


**Figure 7:** Model of orthorhombic structure  $\text{WO}_3$  unit cell and XRD spectrum (W – blue; O – Red)

Miller indices included for the orthorhombic structure. [after ref. 20]

**Table 1.2:** Orthorhombic  $\text{WO}_3$  atomic coordinates represented in unit cell lengths with lattice parameters of  $a = 7.341 \text{ \AA}$ ,  $b = 7.570 \text{ \AA}$ , and  $c = 7.754 \text{ \AA}$  [after ref. 17]

Coordinates /Atom	X	Y	Z
$\text{W}_1$	0.25	0.029	0.031
$\text{W}_2$	0.25	0.030	0.0532
$\text{O}_1$	0	0	0
$\text{O}_{1'}$	0.5	0	0
$\text{O}_2$	0	0	0.5
$\text{O}_{2'}$	0.5	0.5	0
$\text{O}_3$	0.25	0.269	0.027
$\text{O}_4$	0.25	0.278	0.471
$\text{O}_5$	0.25	0.004	0.262
$\text{O}_5$	0.25	0.015	0.776

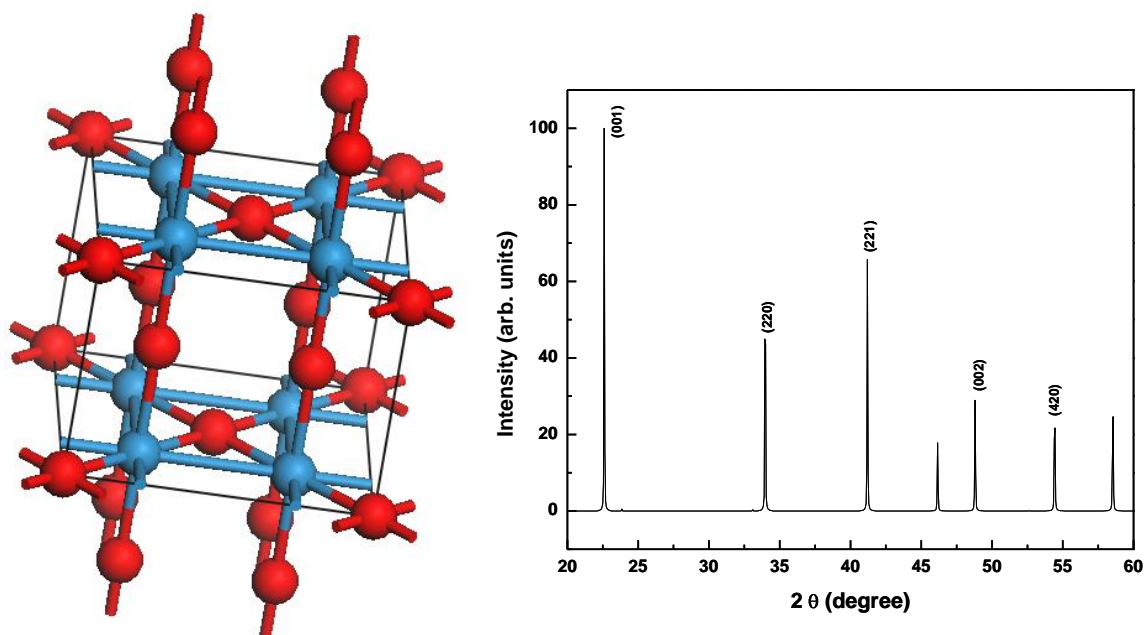


**Figure 8:** Model of Tetragonal  $\text{WO}_3$  unit cell and XRD spectrum (W – Blue; O – Red) Miller indices included for the tetragonal structure. [after refs. 18,19]

**Table 1.3:** Tetragonal  $\text{WO}_3$  atomic coordinates represented in unit cell lengths with lattice parameters of  $a = 5.295 \text{ \AA}$  and  $c = 3.928 \text{ \AA}$  for tetragonal phase of  $\text{WO}_3$ . [after refs. 18,19]

Coordinates /Atom	X	Y	Z
$\text{W}_1$	0.250	0.250	0.0664
$\text{O}_{x1}$	0.250	0.250	0.494
$\text{O}_{y1}$	0	0	0

It is easily seen by analysis of the structure and diffraction spectrum of the tetragonal phase that it has much higher symmetry and fewer diffraction peaks. However, when plotted together the diffraction peaks of the monoclinic, orthorhombic and tetragonal are very similar, such that the separation among the strongest peaks is slight, where the  $2\theta$  values range from about  $23^\circ$  to  $25^\circ$ . This is shown in Figure 9, where the monoclinic, orthorhombic, and tetragonal structure diffraction peaks have been plotted together over the  $2\theta$  region  $22^\circ - 26^\circ$ . This is a known attribute and a point of debate in the community.[21,22].

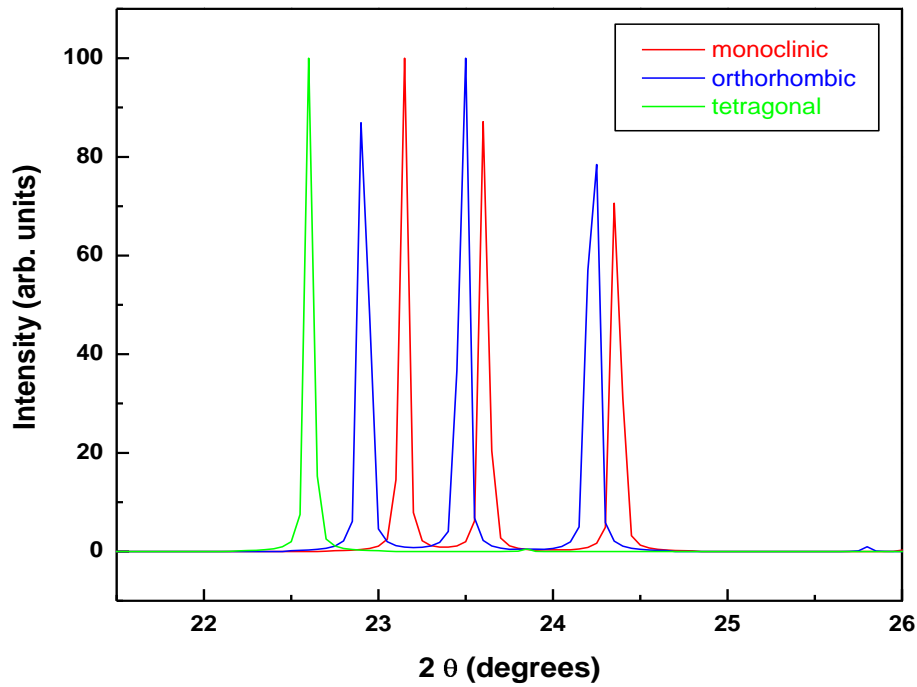


**Figure 9:** Characteristic X-ray diffraction spectra for monoclinic (red), orthorhombic (blue), and tetragonal (green)  $\text{WO}_3$  structures with  $2\theta$  values ranging from about  $22^\circ$  to  $26^\circ$ .

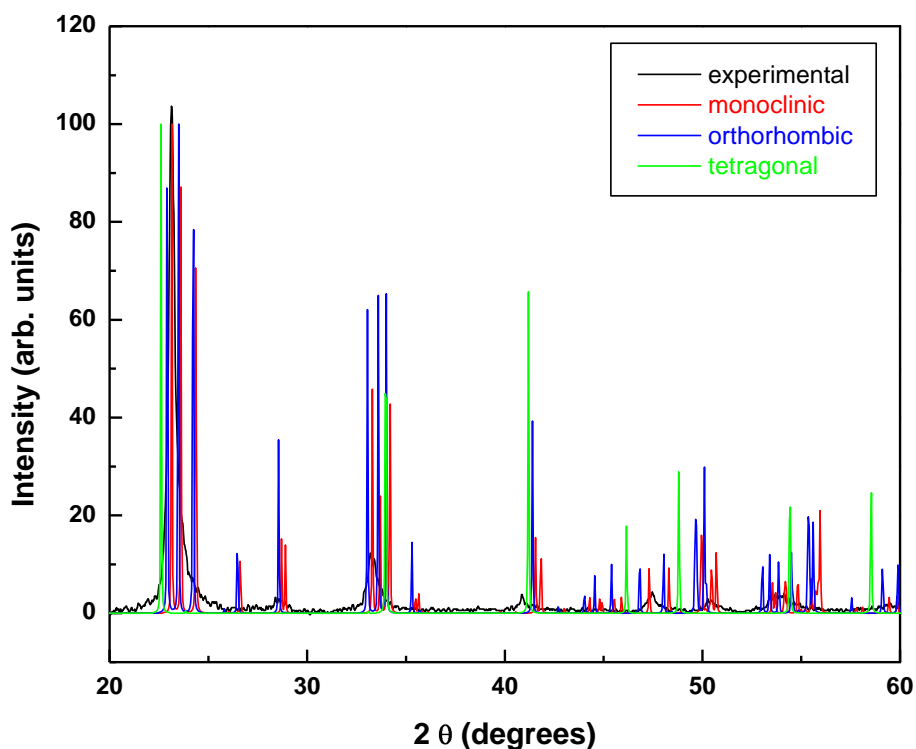


**Figure 10:** Experimental XRD results obtained for pure  $\text{WO}_3$  thin films (black) with characteristic X-ray diffraction spectra for monoclinic (red), orthorhombic (blue), and tetragonal (green)  $\text{WO}_3$  structures.

A thorough XRD was performed on one of the samples. As has been reported earlier, it is a well known phenomenon that annealing a  $\text{WO}_3$  sample causes a change in the morphology of a thin film implying a structural change. This transformation occurs between 330 °C and 740 °C. Regarding one of our  $\text{WO}_3$  samples that were grown on a Si substrate that was heated to a temperature of 500 °C during growth, it is expected that we may have structural changes. Assignment of structural configuration is difficult at best, and could be controversial as one would expect a structure change from monoclinic to orthorhombic; however, a mixture of phases may also exist.

This XRD data is plotted with the computational XRD data for monoclinic, orthorhombic, and tetragonal structures. The difficulty in assigning a structure would only have been amplified if powder

samples had been used and a widening of the peaks would have occurred. For this case, the materials must be thin film with their favored growth ability, and XRD measurements should be exact and careful if an assignment of structure configuration is to be attempted.

Figure 11 shows the computational XRD spectrum for 3% Titanium doped  $\text{WO}_3$  plotted with the computational spectra of  $\text{WO}_3$  monoclinic and tetragonal structures. Peaks and intensities are very similar, however at larger  $2\theta$  angles there are more differences. This is a good step forward, and shows it might be possible to improve  $\text{WO}_3$  to draw out new structural phases by doping with different amounts of Ti.

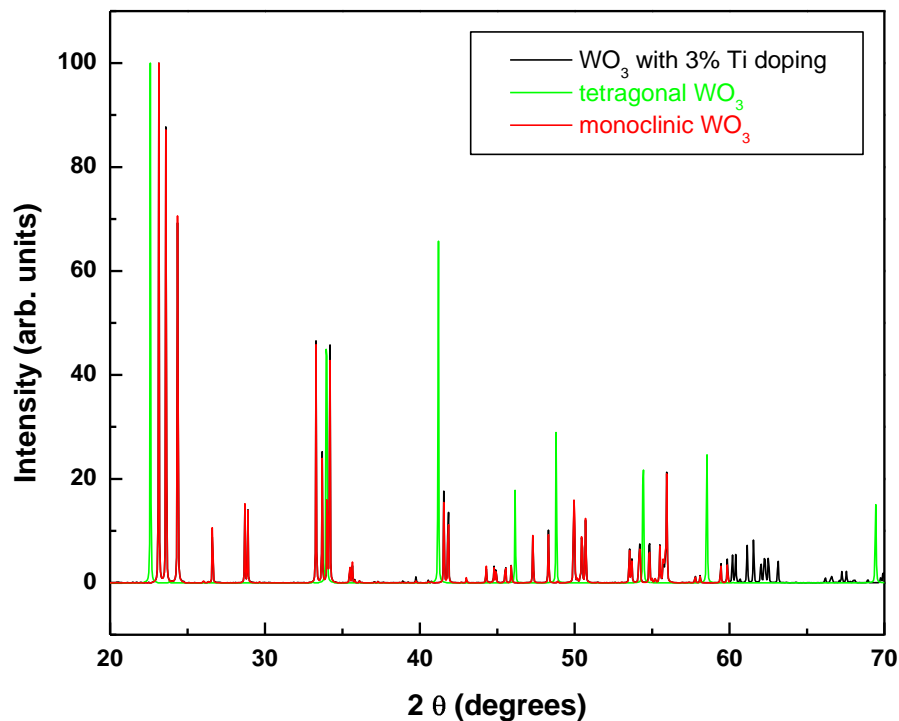


**Figure 11:** XRD spectra for 3% Ti doped  $\text{WO}_3$  (black), monoclinic (red), and tetragonal (green) structures.



Whereas the  $\text{WO}_3$  crystal structure is known and well studied {19-22}, less information is available for Ti-W-O morphology. An accurate assignment of this new material morphology is further complicated by the fact that the strongest diffraction peaks for monoclinic, orthorhombic, and tetragonal  $\text{WO}_3$  structures are very slightly separated, with  $2\theta$  values ranging from about  $23^\circ$  to  $25^\circ$ . In addition, if thin films versus powder samples are considered, the assignment is even more difficult due to the broadness of the XRD peaks and to the film preferential growth direction. These computational analyses are presented and discussed more below.

### **3.3.0 Computational XRD analysis of $\text{WO}_3$ with different Ti doping amounts**

Calculations were done using the software MOPAC2012 {32}. This software introduced new parameterizations for models, to include heavy atoms like Tungsten (Parameterization Model 7, PM7). We used a semi-empirical Molecular Orbital method based on Dewar and Thiel's version of the Neglect of Diatomic Differential Overlap (NDDO) approximation {30}.

Any phase of  $\text{WO}_3$  that is interesting is a deformation of a cubic perovskite-like lattice where tungsten exists with 6 neighbors on three orthogonal axes. A  $4 \times 4 \times 4$  super cell was built. The Geometry of the system was optimized and the lattice vectors and the fractional coordinates of the atoms were allowed to vary and obtain the optimal structure (192 O and 64 W, with 0,1,2,... W atoms substituted with Ti). We used a software called, PowderCell 2.4 written by G. Nolze and W. Kraus {32} in order to create diffraction spectra for the optimal structure geometries.

As can be observed in the theoretical X-ray diffraction spectra of pure  $\text{WO}_3$  versus a 1.5% Ti doping of  $\text{WO}_3$  the Ti doping served to shift the diffraction spectra to lower  $2\theta$  values. It also served to decrease the intensity of the diffraction lines. The implication is an increased disorder within the system. An automatic question would be to ask exactly at what percentage of Ti doping would the influence over the diffraction peaks be impacting negatively.

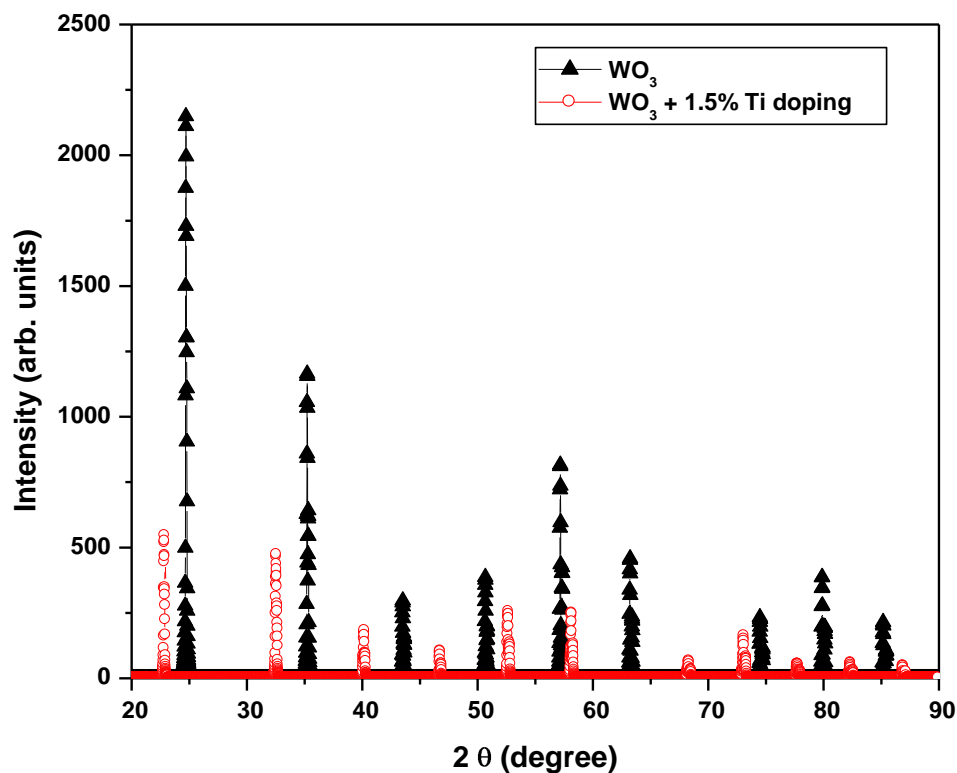


**Figure 12:** Theoretical X-ray diffraction spectra of  $\text{WO}_3$  and 1.5% Ti doped  $\text{WO}_3$ .

Continuing to increase the Ti doping percentage impacted the computed X-Ray diffraction spectra such that the increased percentage correlates to a decrease in the intensity of the peaks, however, impact on the diffraction position is less dramatic. This can be seen in Figure 13 where XRD spectra for different doping percentages are plotted on the same graph. Percentages higher than the 1.5% tend to push the peaks to higher  $2\theta$  values.

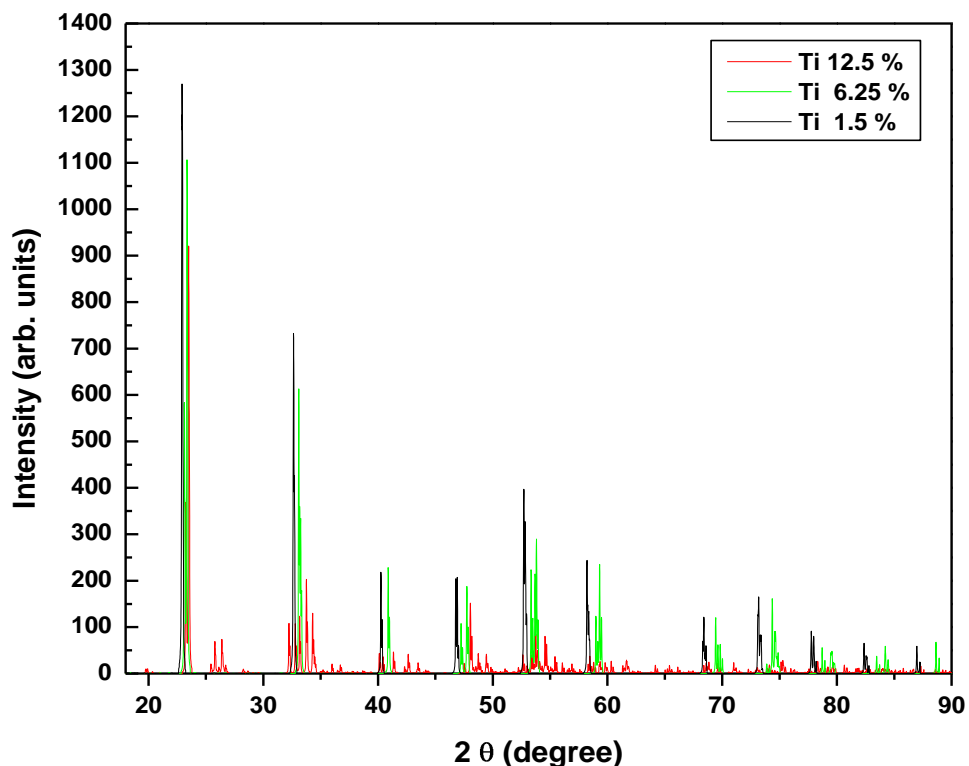


**Figure 13:** Computed XRD spectra for Ti doped  $\text{WO}_3$  at the following percentages 12.5% (red), 6.25% (green), and 1.5% (black) of Ti.

### 3.4.0 Correlation of computed and experimentally obtained XRD results for 5% Ti doping

We now want to compare the experimental findings versus theoretical; specifically we show XRD data, both experimental and theoretical, in Figure 14. The simulated results are for 6.25% Ti doping, the experimental results are with 5% Ti doping.

In order to correlate the experimental findings with theoretical outcomes, we present data in Figure 14. Computationally 6.25% is the nearest mathematically possible percentage per supercell to that of the available Ti-doping thin films we were able to grow.

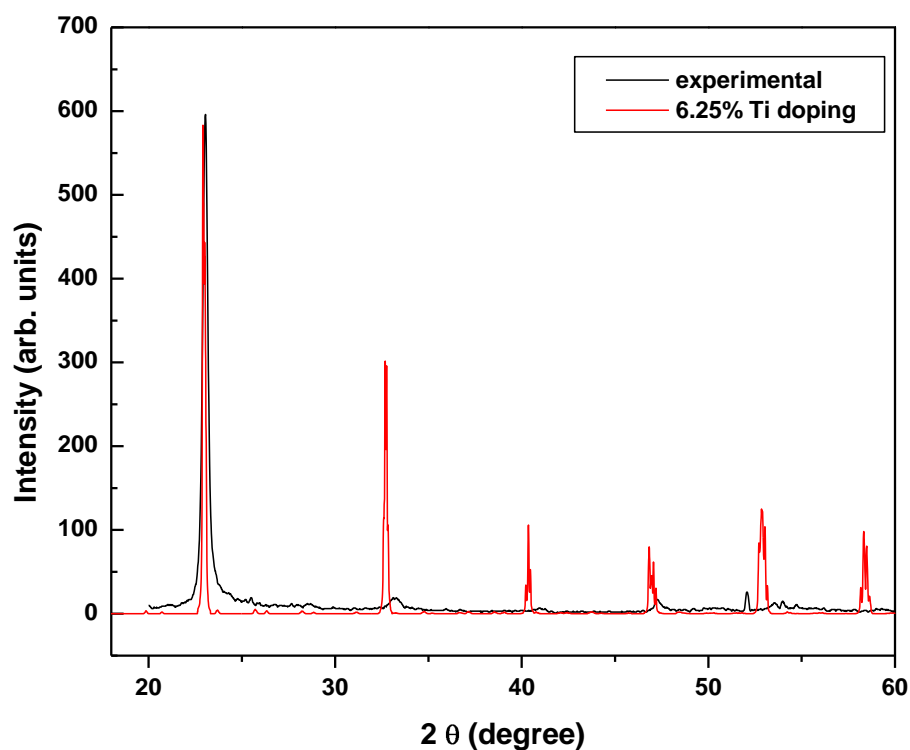


**Figure 14:** XRD spectra for experimental and simulated data for 5% Ti doping (black) and 6.25% Ti (red) of  $\text{WO}_3$ .

Shown in the results we can see that the experimental data show only one diffraction peak that matches the experimental, and that is at a low angle. At higher angles there are weak diffraction features to be analyzed. In general this demonstrates good agreement in the data sets that is within the expected error limits; this is a good correlation between the experimental 5% doping and simulated 6.25% doping.

One of the final goals is to achieve tetragonal morphology in the material. This is not yet attained with this and lower percentages of Ti Doping. We would like to see if higher doping percentages will reproduce said morphology. Figure 15 presents the theoretical XRD spectra of 12.5% doping with the theoretical XRD spectra of tetragonal  $\text{WO}_3$  morphology. This allows a visual comparison of the data, which should be easier.

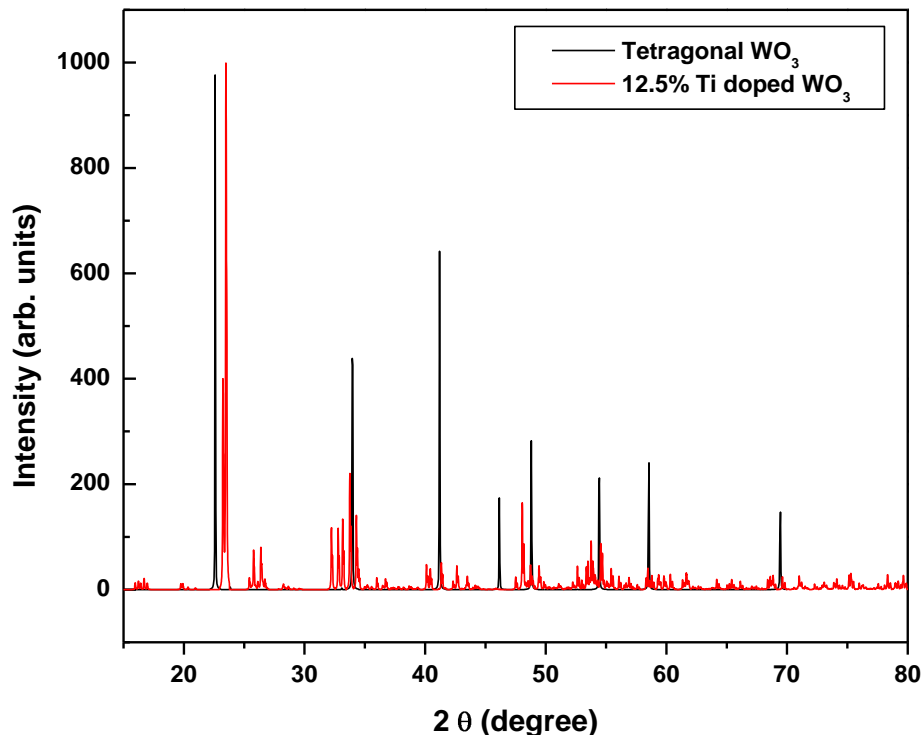


**Figure 15:** Theoretical XRD spectra for  $\text{WO}_3$  with 12.5% Ti doping (red) and for the tetragonal  $\text{WO}_3$  morphology (black).

Now comparing figures 13 and 14, focusing on the positions of the diffraction lines, it is revealed that the 6.25% doping produces lower values than the 12.5% doping. Combined with the fact that all of the theoretical diffraction lines are at lower values than the experimental ones, we can say that there is a potential to produce a tetragonal structure somewhere between 6.5% doping and 12.5 %. Although the spectra in question show a better correlation of the large angle diffraction peaks, they also have their strongest peaks at larger distances, where both have  $2\theta$  peaks at  $23^\circ$ .

The theoretical conclusion is that there will be morphological changes in the  $\text{WO}_3$  structure. Of course what type of change, and to what extent, is contingent on the amount of Ti doping. What follows is our extension of the theoretical conclusions into experimental testing. The simulations were compared mostly through XRD to analyze the material structure. However, experimentally Raman Spectroscopy

and Fourier Transform Infrared Spectroscopy are useful and sensitive tools used in characterization of materials, in this case depicting structural changes in the  $\text{WO}_3$ .

### **3.5.0 Raman analysis of Ti 8% doped $\text{WO}_3$ thin films**

Raman spectroscopic methods were used to gain optical spectroscopic data to confirm the morphological changes that occurred in the 8% Ti doped  $\text{WO}_3$ . Samples tested were grown on substrates that had temperatures of room temperature (RT), 200 °C, and 400 °C.

These results are presented in Figure 16.

The sample thin films were grown on a silicon wafer. Si wafers are known to be covered in a layer of  $\text{SiO}_2$ . Si has a very high oxidation rate and although the  $\text{SiO}_2$  is unwanted it is unavoidable. This can be seen in the features of the Raman spectra in Figure 16 where the Si-O bonds produce features at 303, 435, 622  $\text{cm}^{-1}$ . There are additional vibrational lines at 675 and 822  $\text{cm}^{-1}$  which we attribute to W-O-W stretching modes of  $\text{WO}_3$ . Comparing the spectra of the 400 °C sample and the RT sample shows no increase in the intensities of the vibrational lines. This suggests an amorphous nature for these samples. We would expect that if the material were continuing its crystallization with the higher substrate temperatures, then we would see the Raman line intensity increase and sharpen.

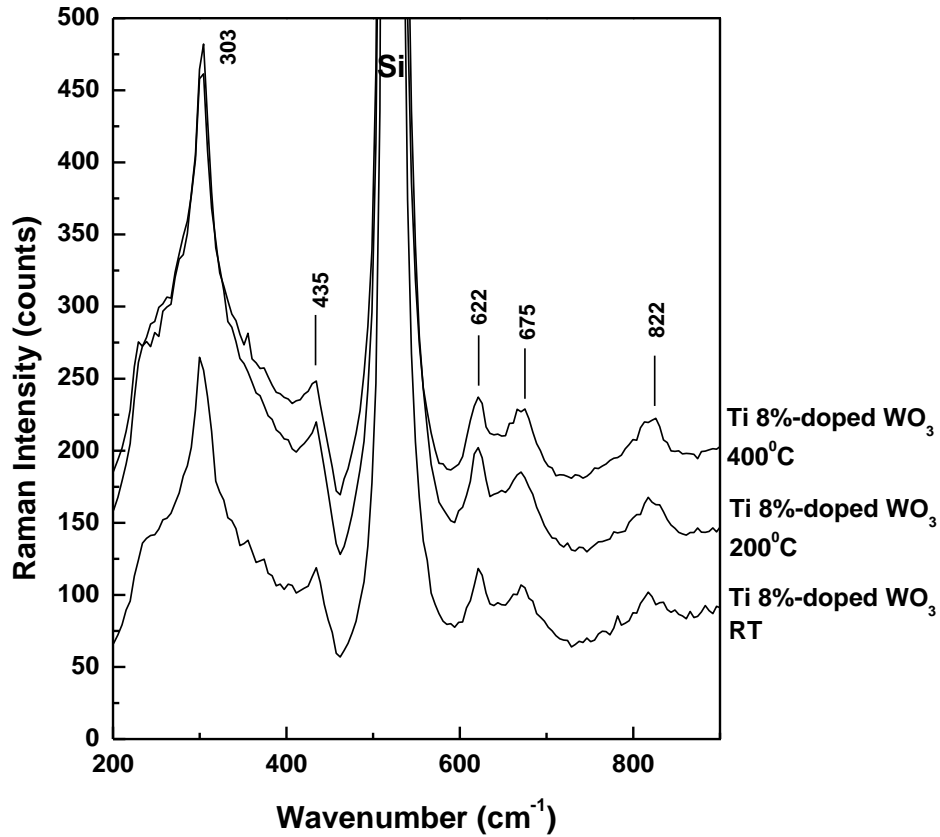


**Figure 16:** 8% Ti Doping Raman Spectra for  $\text{WO}_3$  samples of varying Si substrate growth temperatures, RT, 200 °C, 400 °C.

Experimental Raman data for the 400 °C substrate growth pure  $\text{WO}_3$  samples is plotted simultaneously with the Ti doped results in Figure 17. Doing this allows a direct comparison of the experimental data which leads to an interpretation of morphological changes to  $\text{WO}_3$  structure. It is apparent that the Ti doped  $\text{WO}_3$  samples developed different behaviors in the spectra; we also see that, at similar growth temperatures, the pure  $\text{WO}_3$  samples achieved quicker crystallinity.

For example, both the 8% and 20% Ti doped samples shifted their strong vibrational lines to a frequency about  $10\text{ cm}^{-1}$  above the pure  $\text{WO}_3$  vibrational line at  $810\text{ cm}^{-1}$ ; while the 5% Ti doped sample shifted the  $810\text{ cm}^{-1}$  line to a frequency  $12\text{ cm}^{-1}$  lower, shown in Figure 17. Shifts like this lend themselves to the interpretation that the W-O are being affected in the new Ti doped structure. What can be said is that there is a possibility that as Ti substitutes W in the structure there will be an oxygen deficiency in the structure. So as the doping percentage increases the Ti-O-W chemical bonds get longer as well. In the case of the reduced intensities, they may be caused by the extreme case of elongated chemical bonds, that is, where they may have been broken.

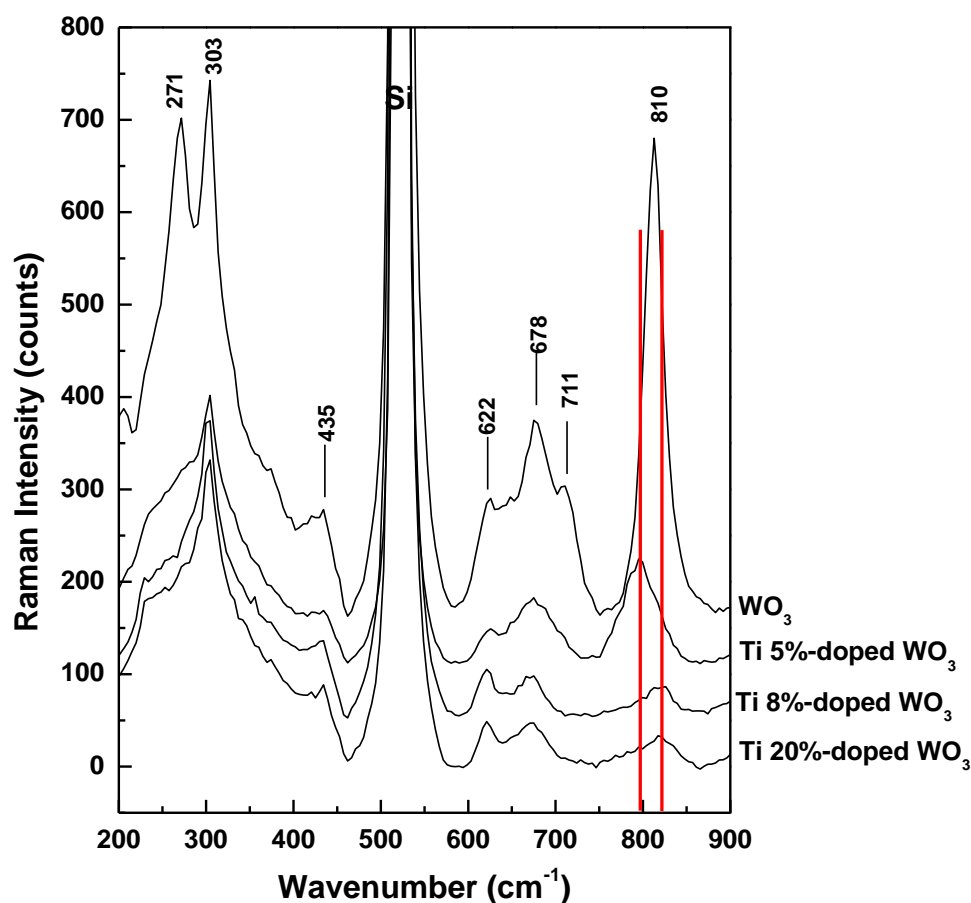


**Figure 17.** Multiple percentage Ti-doped  $\text{WO}_3$  samples' Raman spectra, grown at  $400\text{ }^\circ\text{C}$  substrate temperature.



The spectroscopic band profiles of all  $\text{WO}_3$  samples doped with Ti saw reduced peak intensities. What follows is computational analysis and behaviors observed, which are attributed to the disorder in the structure of the Ti-doped samples. The amorphous like behavior of the 8% Ti doped thin film samples could be caused by non-optimized growth conditions, or the need for higher sample growth temperatures.

### **3.6.0 Infrared absorption results of Ti 8% doped $\text{WO}_3$ thin films**

The implication of an amorphous structure in the 8% Ti doped  $\text{WO}_3$  samples is further corroborated by comparison of infrared absorption spectra with the other Ti doping percentages. Figure 18 plots the multiple spectra together with the Silicon substrate spectrum for reference.

### **3.7.0 Correlation of computed and experimentally obtained infrared results for Ti doping**

The computational analysis was performed by creating a smaller system due to the fact that infrared vibrational calculations take an order of magnitude more computer time than for a geometrically optimized system. A super cell of 8 W and 24 O atoms was composed as a 2x2x2 cubic primitive cell. Replacing one W atom with a Ti atom represents a 12.5% Ti doping. Normal modes of vibration were calculated using geometric optimization in this analysis. For atoms in the super cell let us take  $N = 32$ , with  $3N - 6 = 90$  non-zero modes, all positive. Negative frequencies would only exist in Non-optimal geometries. MOPAC2012 calculated the transition dipole of modes. The transition dipole of modes is proportional to the relative intensity of an infrared active band. This was used in creating the theoretical IR spectra of both the 12.5% Ti doped  $\text{WO}_3$  and pure  $\text{WO}_3$ . They are plotted using a width of  $5 \text{ cm}^{-1}$  for each vibration

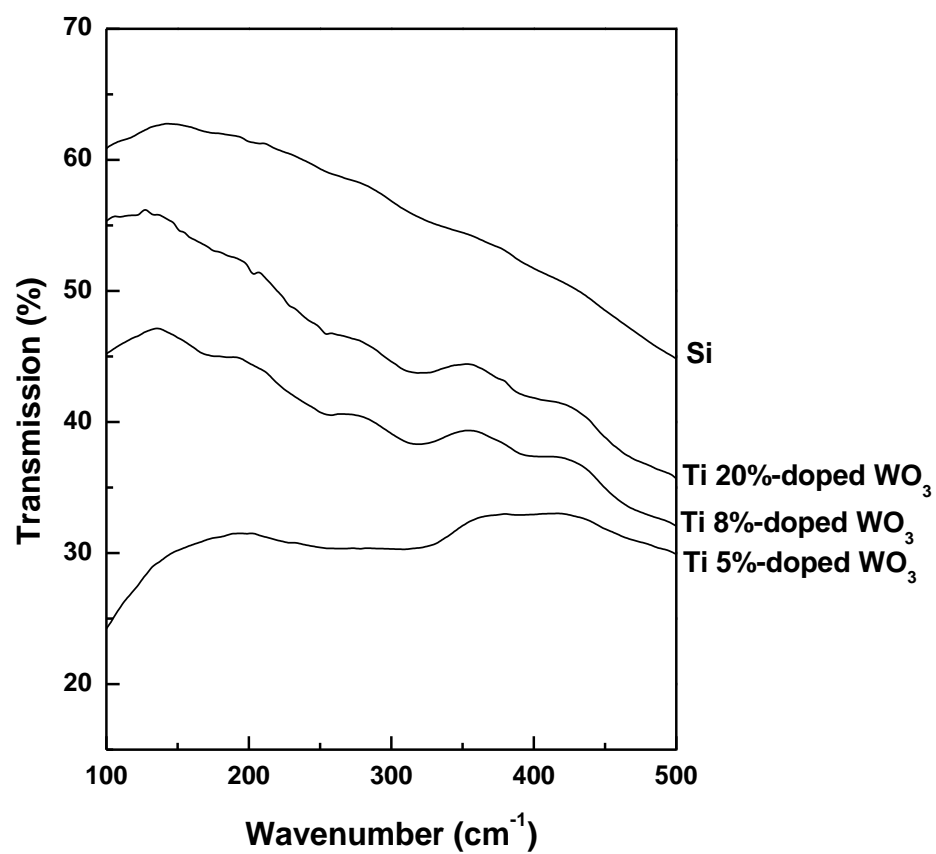


**Figure 18.** Pure WO<sub>3</sub> and Ti-doped WO<sub>3</sub> IR absorption spectra for samples grown at 400 °C substrate temperature.

As before we compare theoretical and experimental absorption infrared vibrational lines and transmission data for 12.5% Ti doping and pure  $\text{WO}_3$ , they are plotted together in Figure 19.

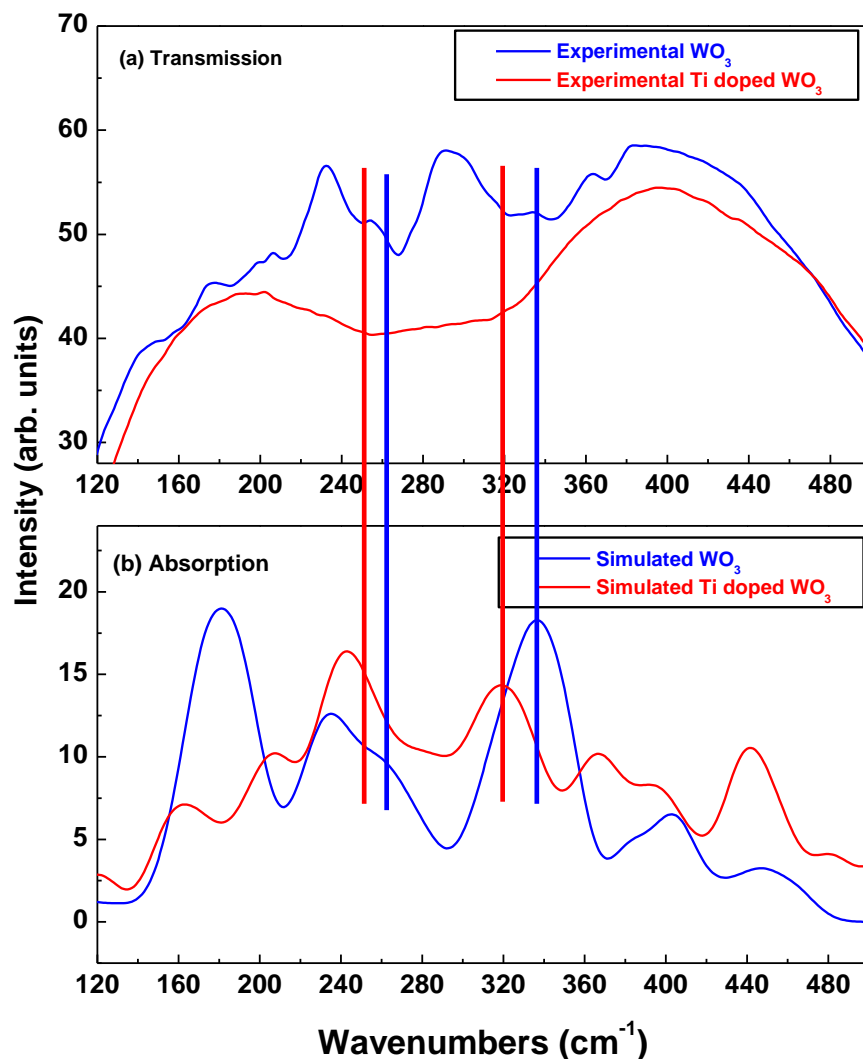


**Figure 19:** (a) Experimental transmission data for pure  $\text{WO}_3$  (blue) and 5% Ti doping of  $\text{WO}_3$  (red)  
 (b) Simulated absorption infrared vibrational lines for pure  $\text{WO}_3$  (blue) and 12.5% Ti doping of  $\text{WO}_3$  (red).

Experimental measurements were only able to be carried out on the 5% Ti doped samples. This is unfortunate; however comparison of the vibrational lines shows a positive correlation between the calculated and measured results regardless of the actual percentage of Ti doping. Correlation is evident between the blue and red lines. Ti incorporation into a  $\text{WO}_3$  structure shifts frequencies in the spectra even though the features are broad, they are still noticeable. Similar results were observed previously using Raman spectroscopy {16,17}

### **3.8.0 Concluding remarks**

Theoretical calculations imply that it is possible to get the desirable higher symmetry structure using higher Ti doping percentages. However the outcome of his work shows that the best amount of Ti doping is 5% using the growth methods outlined here. This study serves to confirm that the Ti 8% doping induces significant disorder in the system.

## Chapter 4: Conclusion

### 4.1.0 Concluding remarks

Metal oxides like Tungsten Oxide ( $\text{WO}_3$ ) are well documented and characterized in the literature, with uses in darkening windows and mirrors, flat computer displays, solar panel cooling, and sensors (the interest in this study). Though synthesized in 1841,  $\text{WO}_3$  is used today in all kinds of ways using its ability to darken with an electrical current to limit the amount of sunlight that reaches surfaces. It can protect solar cells, or keep our houses cool thus causing a drop in energy consumption. For the purpose of this study our focus was on the characterization of Ti doping of  $\text{WO}_3$  thin films. This is of great interest in industry. New and better sensor materials are needed to keep up with demand as the world consumes more and more power requiring bigger or just more power producing stations. The increases in energy production are of concern due to environmental impact. Poison gasses are a byproduct of this; as such sensors and sensing materials are absolutely necessary. However, characteristics and sensing properties all stem from the materials' stoichiometry, nano-structures, grain size, nanoporosity, and so many other properties of materials. In this study we explore the spectroscopic, structural, and well known properties of  $\text{WO}_3$  alongside experimental explorations of both pure and Ti doped  $\text{WO}_3$ .

Ti doping of  $\text{WO}_3$  is less documented and the focus of this study. In order to test this material, sample thin films of pure  $\text{WO}_3$  and varying Ti doped  $\text{WO}_3$  were prepared using Radio Frequency magnetron sputtering (RF) (13.56 MHz) to grow thin films on a silicon substrate. Synthesis of the thin films began with a silicon substrate that was cleaned and dried, then introduced into a vacuum chamber with metal targets made of tungsten or tungsten-titanium alloy in percentages appropriate for testing. Metal targets were sputtered in an argon atmosphere where oxygen flow was regulated via mass flow sensors.

This study aims to compare multiple Ti doping percentages in  $\text{WO}_3$  theoretically and then compare with experimental data taken from thin films of various Ti doping grown at temperatures ranging from room temperature to  $400\text{ }^{\circ}\text{C}$ . A phenomenon has occurred in previous studies where sensitivity of a metal oxide was increased by annealing the sample. What was found was that sensing materials change their electrical properties when atmospheric gasses interact with oxygen at the surface. Annealing and high growth temperatures change the topology of the thin film from flat to grainy. The increase in surface area correlates with an increase in sensitivity to the target gases. In addition to this Ti doping is seen as an impurity that can enhance the materials' ability to withstand higher temperatures in addition to changing the ratio of  $\text{W}^{+4}$  and  $\text{W}^{+5}$ . The temperatures in a coal gasification plant atmosphere reach upwards of  $800\text{ }^{\circ}\text{C}$ . Sensing material in that environment must be robust enough to handle that temperature. Ti doped  $\text{WO}_3$  has that potential.

Characterization of the materials was to be conducted using Fourier Transform Infrared Spectroscopy, Raman Spectroscopy, X-ray diffraction, and other theoretical and simulated approaches. A theoretical approach, in which we developed XRD spectra for different optimized geometries, offered a basis of comparison for experimental XRD data. Once samples of varying doping percentage were in hand, the samples were tested using FTIR absorption spectra and Raman spectra. Although it is understood in the study that surface topology changes would imply more surface sites for gases to react with, atomic force microscopy would offer little to the study as it would be unable to expose the underlying structure. In this case Raman spectra were used for their ability to reveal vibrational modes that would expose the structure of the material and thus be comparable to theoretical modes calculated. Raman Spectroscopy was performed with an Alpha 300R WITec Confocal Raman system with a 532 nm excitation of a Nd:YAG laser. Fourier Transform Infrared Spectroscopy was performed on a Bruker IFS 66v system.

Theoretical calculations optimized Ti doping at somewhere between 6.25% and 12%.

Experimental data infers that under the given growing conditions optimal Ti doping is 5%. Once all data sets are considered it is apparent that the addition of Ti to a  $\text{WO}_3$  sample develops different behaviors in the spectra contingent on Ti doping. For example it was shown that 5% Ti doping shifted peaks to lower values, and 8% and 20% Ti doping shifted peaks higher. Intensity also suffered with progressive doping. In the end the real outcome is that the theoretical calculations placed optimal Ti-doping at somewhere between 6.75% and 12.5%. However the experimental result is that the optimal Ti-doping of the grown thin films for this study produced optimal results at the 5% Ti doping.

Annealing of samples grown at 400  $^{\circ}\text{C}$  post-growth has no positive impact on the thin film structure. It is suspected that higher growth temperatures may allow the percentage of Ti to be increased and the material retain desired characteristics. Further study would be necessary but is beyond the scope of this research.

## References

- {1} Clean Coal Technologies for Power Generation, P. Jayarama Redd
- {2} Minchener, A. J., Coal Gasification for Advanced Power Generation (2005)
- {3} K. Huang, Q. Zhang, F. Yang, D. He, *Nano-Res*, vol. 3, 281-287 (2010).
- {4} W. Gopel, K. Schierbaum, *Sensors, Volume 2: Chemical and Biochemical Sensors*, Winheim, p.2 (1991).
- {5} Reddy, Jayarama P., *Clean Coal Technologies for Power Generation*, CRC Press, (2014)
- {6} N. Basan, U. Weimar, Understanding the fundamental principles of metal oxide gas sensors; the example of CO sensing with SnO<sub>2</sub> sensors in the presence of humidity, *J. Phys.: Condens. Matter*, vol. 15 R813-839, (2003).
- {7} V. Smatko, V. Golovanov, *Structural stability of In<sub>2</sub>O<sub>3</sub> films as sensor materials*, 2009, Springer Science+Business Media.
- {8} M. Ferroni, V. Guidi, G. Martinelli, *Characterization of a nanosized TiO<sub>2</sub> gas sensor*, *Nanostructure Materials*, vol. 7, 709-718 (1999)
- {9} NIOSH/OSHA: Occupational Health Guidelines for Chemical Hazards, National Institute for Occupational Safety and Health/Occupational Safety and Health Administration, January 1981.
- {10} Takeda, Hiromitsu, Adachi Kenji, Near Infrared Absorption of Tungsten Oxide Nanoparticle Dispersions, *J. Am. Ceram. Soc.*, 90 [12] 4059–4061 (2007)
- {11} Lee San Bing, The annealing effects of tungsten oxide interlayer based on organic photovoltaic cells; *Solar Energy Materials*, v. 117 no. , pp. 203-208 Date: 2013-10-01



{12} M.D. Antonik, J.E. Schneider, E.L. Wittman, K. Snow, J.F. Vetelino, R.J. Lad; Microstructural effects in WO<sub>3</sub> gas-sensing films; Thin Solid Films; Volume 256, Issues 1–2, Pages 1-280 (1 February 1995)

{13} D. J. Smith, J. F. Vetelino, R. S. Falconer and E. L. Wittman, *Sensors Actuators B*, 13-14 (1993) 264.

{14}

[http://www.google.com/imgresimgurl=http://www.kosi.com/Raman\\_Spectroscopy/images/tutorial4.gif&imgrefurl=http://www.kosi.com/Raman\\_Spectroscopy](http://www.google.com/imgresimgurl=http://www.kosi.com/Raman_Spectroscopy/images/tutorial4.gif&imgrefurl=http://www.kosi.com/Raman_Spectroscopy)

{15} N. B. Colthup, L. H. Daly, and S. E. Wiberley, *“Introduction to Infrared and Raman Spectroscopy”*, 3<sup>rd</sup> ed., Academic Press Inc., San Diego, (1990).

{16} F.S. Manciu, J.L. Enriquez, W.G. Durrer, Y. Yun, C.V. Ramana, and S.K. Gullapalli: *“Spectroscopic analysis of tungsten oxide thin films”*, Journal of Materials Research, vol. 25, Issue 12, 2401-2406 (2010).

{17} Young Yun, Ph.D thesis: *“Microscopic and spectroscopic analysis of WO<sub>3</sub> and Ti-doped WO<sub>3</sub> thin films”*.

{18} Jose Luis Enriquez Carrejo M.S. thesis: *“Spectroscopic analysis of tungsten oxide thin films for sensor applications”*.

{19} S. Tanisaki, *Crystal structure of monoclinic tungsten trioxide at room temperature*, Journal of the Physical Society of Japan, vol. 15, No. 4 (1960).

{20} E.Salje, *The orthorhombic phase of WO<sub>3</sub>*, Acta Cryst. B33, 574577 (1977).

{21} K.R. Locherer and K.H. Salje, *The refinement of a tetragonal phase of WO<sub>3</sub> using a novel PSD high temperature X-ray powder diffractometer*, Phase Transitions, vol. 69, 85-83 (1999).

{22} K.R. Locherer, I.P. Swainson, E.K.H. Salje, *Transition to a new tetragonal phase of WO<sub>3</sub>: crystal structure and distortion parameters*, J. Phys.: Condens. Matter, vol. 11, 4143-4156 (1999).

- {23} L. Sangaletti, L.E. Depero, G. Sberveglieri, B. Allieri, E. Bontempi, S. Groppelli, *Growth of WO<sub>3</sub> crystals from W-Ti-O thin films*. J. Cryst. Growth, vol. 198/199, 1240 (1999).
- {24} M. Boulova and G. Lacazeau, *Crystallite Nanosize Effect on the Structural transitions of WO<sub>3</sub> Studied by Raman Spectroscopy*, Journal of Solid State Chemistry, vol. 167, 425-434 (2002).
- {25} H.-T. Sun, C. Cantalini, L. Lozzi, M. Passacantando, S. Santucci, M. Pelino, *Microstructural effect on NO<sub>2</sub> sensitivity of WO<sub>3</sub> thin film gas sensors. Part 1. Thin film devices, sensors and actuators*, Thin Solid Films, vol. 287, 258-265 (1996).
- {26} E. Cazzanelli, C. Vinegoni, G. Mariotto, A. Kuzmin, J. Purans, *Raman study of the phase transitions sequence in pure WO<sub>3</sub> at high temperature and in H<sub>x</sub>WO<sub>3</sub> with variable hydrogen content*, Solid State Ionics, vol. 123, Issues 14, 67-74, ISSN 01672738, DOI: 10.1016/S01672738(99)001010 (1999).
- {27} Y. Shen, T. Yamazaki, Z. Liu, D. Meng, T. Kikuta, N. Nakatani, *Influence of effective surface area on gas sensing properties of WO<sub>3</sub> sputtered thin films*, Thin Solid Films, vol. 517, 2069-2072 (2009).
- {28} B. Pecquenard, *Orthorhombic WO<sub>3</sub> formed via a Ti-stabilized WO<sub>3</sub>-H<sub>2</sub>O phase*, Journal of Solid State Chemistry, vol. 135, Issue 1 (2002).
- {29} Michael J.S. Dewar and Walter Thiel, "Ground states of molecules. 38. The MNDO method. Approximations and parameters". *Journal of the American Chemical Society* 99 (15): 4899. doi:10.1021/ja00457a00 (1977).
- {30} J. Pople and D. Beveridge, *Approximate Molecular Orbital Theory*, McGraw-Hill, (1970).
- {31} MOPAC2012, James J. P. Stewart, Stewart Computational Chemistry, Colorado Springs, CO, USA, [HTTP://OpenMOPAC.net](http://OpenMOPAC.net) (2012).
- {32} [http://www.ccp14.ac.uk/ccp/web-mirrors/powdcell/a\\_v/v\\_1/powder/details/powcell.htm](http://www.ccp14.ac.uk/ccp/web-mirrors/powdcell/a_v/v_1/powder/details/powcell.htm)

## **Vita**

Aurelio Pàez earned his Bachelor of Science degree in Physics from the University of Texas at El Paso (UTEP) in 2012.

While pursuing his degree, Mr. Pàez worked as a Research Assistant and Teaching Assistant in the department of Physics at UTEP. He co-authored a paper, “Development of Conductive Boron-Doped Diamond Electrode: A Microscopic, Spectroscopic, and Voltammetric Study”. He also became lead T.A. in the physics department where he was responsible for teaching other teaching assistants how to teach students efficiently.

Mr. Pàez has presented research at various conference meetings to include The American Astronomical Society, American Physical Society, and the COURI Symposium at UTEP.

Mr. Pàez has received several awards for research and his teaching, to include an award from UTEP COURI 2012 in Bioinformatics and Modeling and department recognition for teaching excellence, twice.

Permanent address: 7608 Highway 28  
Anthony, NM, 88021

This thesis was typed by Aurelio Pàez.